

THE PHOTOMETRIC AND KINEMATIC STRUCTURE OF FACE-ON DISK GALAXIES. III. KINEMATIC INCLINATIONS FROM H α VELOCITY FIELDS

DAVID R. ANDERSEN¹ AND MATTHEW A. BERSHADY²

¹ NRC Herzberg Institute of Astrophysics, 5071 W Saanich Road, Victoria, BC V9E 2E7, Canada; david.andersen@nrc-cnrc.gc.ca

² Department of Astronomy, University of Wisconsin, 475 N Charter Street, Madison, WI 53706, USA; mab@astro.wisc.edu

Received 2012 October 4; accepted 2013 February 28; published 2013 April 12

ABSTRACT

Using the integral field unit DensePak on the WIYN 3.5 m telescope we have obtained H α velocity fields of 39 nearly face-on disks at echelle resolutions. High-quality, uniform kinematic data and a new modeling technique enabled us to derive accurate and precise kinematic inclinations with mean $i_{\text{kin}} = 23^\circ$ for 90% of these galaxies. Modeling the kinematic data as single, inclined disks in circular rotation improves upon the traditional tilted-ring method. We measure kinematic inclinations with a precision in $\sin i$ of 25% at 20° and 6% at 30° . Kinematic inclinations are consistent with photometric and inverse Tully–Fisher inclinations when the sample is culled of galaxies with kinematic asymmetries, for which we give two specific prescriptions. Kinematic inclinations can therefore be used in statistical “face-on” Tully–Fisher studies. A weighted combination of multiple, independent inclination measurements yield the most precise and accurate inclination. Combining inverse Tully–Fisher inclinations with kinematic inclinations yields joint probability inclinations with a precision in $\sin i$ of 10% at 15° and 5% at 30° . This level of precision makes accurate mass decompositions of galaxies possible even at low inclination. We find scaling relations between rotation speed and disk-scale length identical to results from more inclined samples. We also observe the trend of more steeply rising rotation curves with increased rotation speed and light concentration. This trend appears to be uncorrelated with disk surface brightness.

Key words: galaxies: kinematics and dynamics – galaxies: spiral – galaxies: structure

Online-only material: color figures

1. INTRODUCTION

This paper addresses the close connection between the accuracy of estimating inclinations and the presence of kinematic asymmetries in dynamical studies of nearly face-on disk galaxies. The connection is particularly relevant because the study of disk galaxy velocity fields have yielded important clues into galaxy structure and dynamics, and their measurements have been extended to high redshift (e.g., Förster Schreiber et al. 2009; Law et al. 2009; Wright et al. 2009). At the most basic level, the discovery of flat, extended rotation curves is perhaps the most compelling proof for the ubiquitous existence of dark matter (e.g., Freeman 1970; Rubin et al. 1980; Bosma 1981; Begeman 1989; Verheijen & Sancisi 2001; de Blok et al. 2008). In this context, the important element of a velocity field for spiral disks is the major axis position–velocity relationship, i.e., the rotation curve. Equally as important is the disk inclination, required to convert projected velocity to rotation speed and dynamical mass.

The Tully–Fisher relation between the luminosity and rotation speed of spiral galaxies (Tully & Fisher 1977, hereafter TF) is also directly related to velocity fields. The TF relation can be re-couched as a physical relationship between the baryons responsible for luminosity and the dynamical galaxy mass dominated by dark matter. While the TF relation can be measured with only line widths and luminosities, detailed velocity fields are required to refine the TF relationship (e.g., by down-selecting based on rotation-curve shape; Verheijen 2001), to better understand the scatter in the TF relationship due to departures from simple circular motion, and to make detailed assessments of the dynamical state of galaxy disks. Here again inclination plays a critical role.

While TF and rotation-curve studies need not (and generally do not) target galaxies at low inclination, for estimating the dynamical mass of galaxy disks using stellar dynamical tracers (e.g., the DiskMass Survey; Bershady et al. 2010a), a careful balance must be achieved in the projection of disk rotation and the vertical stellar oscillation. The optimum inclination is roughly 30° (Bershady et al. 2010b), which is quite low.

In terms of disk asymmetry studies, velocity fields have been used to study elliptical orbits in disks and quantify the frequency of warps (Bosma 1981; Briggs 1990; Schoenmakers et al. 1997; Swaters et al. 1999; Angiras et al. 2007; Sellwood & Sánchez 2010; Guijarro et al. 2010). Studies of disk asymmetry find roughly 50% of galaxies have $m = 1$ modes (lopsidedness) in either the distribution of gas or their velocity fields (Baldwin et al. 1980; Haynes et al. 1998; Kornreich et al. 2000; Andersen & Bershady 2009; Espada et al. 2011), implying that asymmetries are maintained for several rotation time scales or that galaxy harassment is very common in the field (Richter & Sancisi 1994; Jog 1999). While a few studies have included disks observed at low inclinations (Kornreich et al. 2000; Kranz et al. 2001; Chemin et al. 2006; Epinat et al. 2008; Neumayer et al. 2011), most kinematic studies of disk galaxy kinematics have been done at $i > 45^\circ$. This is a limitation. It is important to study kinematic asymmetries at lower inclinations because (1) the link between kinematic and photometric asymmetries can be explored (most photometric studies of disk asymmetry are performed on nearly face-on galaxies; e.g., Zaritsky & Rix 1997); (2) projection effects and extinction are minimized in face-on disks; and (3) kinematic asymmetry studies at low inclinations probe non-planar asymmetries as opposed to non-circular asymmetries that can be studied for more inclined spiral galaxies (Kornreich et al. 2000).

Hence in both cases—asymmetry studies and dynamical estimates of galaxy disk *and* total mass—a reliable and accurate measure of inclination at low inclination is of the essence. It is also particularly desirable that the inclination measurement be independent of the **TF** relation. This independence would enable, e.g., an assessment of scatter in the **TF** relation due to kinematic asymmetries or variations in disk mass-to-light ratios. The development of an improved method for measuring kinematic inclinations in this paper was directly motivated by these needs.

In previous work, mostly inclined galaxies have been chosen for **TF** and asymmetry studies primarily because traditional photometric or kinematic methods for determining inclinations fail for nearly face-on systems. In the nearly face-on regime, photometric axis ratios fail to deliver reliable inclinations because spiral structure perturbs the nearly circular isophotes. The traditional kinematic method consists of fitting a set of radially nested, but independently tilted rings to the observed velocity field. This method fails because there becomes an increasingly large covariance between rotation speed and inclination at small inclinations (Begeman 1989). The covariance is primarily due to the limiting precision of the velocity measurements, but limitations on the kinematic method also arise due to the presence of non-circular motions. However, the application of fitting tilted rings typically down-weights or excludes data at azimuthal angles away from the kinematic major axis to mitigate the impact of disk warping on *accuracy* (Begeman 1989). This mitigation is often important for H I studies because H I, in contrast to H α , often extends to large radii where warps are prevalent (Briggs 1990; Saha et al. 2009; Christlein et al. 2010). However, this down-weighting reduces the *precision* not only because less of the data is used but because, as we will show, the difference between velocity-field models with different inclinations is maximized at angles intermediate between major and minor kinematic axes.

The reasoning behind the tilted-ring approach is well motivated by kinematic studies using H I data because the relatively low spatial resolution of the beams, or H I holes in the center of disks preclude the inner regions of disks for kinematic measurements, while at large radii warping of disks is often appreciable (e.g., Saha et al. 2009). Most kinematic studies of spiral disk velocity fields have been done in H I. H I observations are advantageous because they allow for studies of gas out to large radii, although H I is sometimes depleted in central regions because gas is either ionized or in the molecular phase. Consequently, H α velocity fields offer a complimentary view of galaxy disks because H α velocity fields typically sample the inner regions of disks at higher spatial resolution while they do not extend to large radii. They have been used to study substructure in disk galaxies including streaming motions of ionized gas in spiral arms (e.g., Rozas et al. 2000; Kranz et al. 2001; Chemin et al. 2006; Fathi et al. 2007; Neumayer et al. 2011). H α observations also are typically more efficient given extant observing facilities, as the required observations are often times shorter than H I observations.

One question which arises is whether the past and current limitations of H I synthesis maps have overly restricted previous kinematic surveys in inclined systems. Specifically, since the inner regions of typical disks (out to several scale lengths) are not significantly warped, with higher-resolution optical kinematic data, it may be possible to use these data more effectively to constrain inclination. We will show that in this case it is possible to adopt a rotation model with a single disk geometry, i.e., a tilted

disk, with no down-weighting or exclusion of data aside from the usual weighting by observational error. This approach has the distinct advantage of combining as much of the signal as possible to constrain a single geometry. Moreover, at small radii where the rotation curve is not flat, there is a covariance between rings that increases the constraints on inclination. In total, these two factors make it possible to reasonably constrain the kinematic inclination of disks down to inclinations of $i \sim 15^\circ$ and use these inclinations to better understand the nature of galaxy disks.

In this paper, we begin by describing the kinematic data and our method for producing velocity fields in Section 2. We demonstrate the ability to fit single, inclined, circular velocity-field models to these kinematic maps in Section 3, and show that the inclinations derived from these models are accurate and precise. In Section 4, we examine the residual velocity-field structure and present projected rotation curves, and measures of rotation-curve and kinematic asymmetries. In Section 5, we compare different methods of estimating inclination from kinematics, surface photometry, and inverting the **TF** relation, and evaluate their performance in light of the presence of kinematic asymmetries. In this section, we also characterize rotation-curve shape and show that the steepness of the rotation-curve rise correlates with the amplitude of the terminal velocity, the photometric scale length of the disk, image concentration, and surface brightness. Finally, we summarize and discuss our results in Section 6. The ability to measure accurate and precise inclinations, coupled with some critical measurements from imaging data, is crucial to our ability to measure disk ellipticity (D. R. Andersen & M. A. Bershady, in preparation).

2. DATA

2.1. Integral Field Spectroscopy

We have collected H α integral field spectroscopy from DensePak on the 3.5 m WIYN telescope³ for 39 nearby, nearly face-on disk galaxies. The description of the data and basic reductions and analysis are described in Andersen et al. (2006; Paper I).

For this paper, the data product from Paper I in which we have the greatest interest here is the line centroid. This is measured from the resolved H α lines by fitting a Gaussian; in a large fraction of the cases, a Gaussian is a good fit to the line and provides an excellent measurement of the centroid. The error on the centroid is extracted from the covariance matrix. A visual inspection of the line fits was used to disqualify multiple component and misfit lines from the analysis performed here.

2.2. Surface Photometry

Broadband imaging is a critical complement to the spectroscopic data for several reasons. In this paper, we use *R*-band images ($\lambda_{\text{eff}} = 7000 \text{ \AA}$) to compare to DensePak continuum measures ($\lambda_{\text{eff}} = 6800 \text{ \AA}$) as an independent check on our ability to register the Integral Field Unit (IFU) data in an astrometric sense. We also use the data to estimate the photometric inclination and measure total magnitudes. In earlier papers, we have used the same data to estimate the intrinsic disk ellipticity (Andersen et al. 2001) and to construct a **TF** (Tully & Fisher 1977) relation for nearly face-on galaxies (Andersen & Bershady 2003).

³ The WIYN Observatory is a joint facility of the University of Wisconsin–Madison, Indiana University, Yale University, and the National Optical Astronomy Observatories.

Table 1
Photometry

PGC	DM (mag)	R (mag)	I (mag)	A_R (mag)	A_I (mag)	M_R (mag)	M_I (mag)
2162	34.35 ± 0.06	14.08 ± 0.02	13.54 ± 0.02	0.052	0.038	-20.54 ± 0.07	-21.00 ± 0.07
3512	34.35 ± 0.06	13.35 ± 0.02	12.76 ± 0.02	0.086	0.063	-21.31 ± 0.07	-21.81 ± 0.07
5345	32.31 ± 0.15	14.16 ± 0.04	13.76 ± 0.05	0.084	0.061	-18.45 ± 0.16	-18.77 ± 0.16
5673	33.96 ± 0.07	13.30 ± 0.04	12.76 ± 0.05	0.144	0.105	-21.02 ± 0.09	-21.46 ± 0.09
6855	34.12 ± 0.07	13.79 ± 0.05	13.21 ± 0.05	0.224	0.162	-20.77 ± 0.09	-21.23 ± 0.09
7826	32.58 ± 0.14	13.58 ± 0.04	12.98 ± 0.05	0.201	0.146	-19.42 ± 0.14	-19.90 ± 0.15
8941	35.58 ± 0.03	13.44 ± 0.04	12.86 ± 0.05	0.239	0.174	-22.60 ± 0.06	-23.05 ± 0.06
14564	33.37 ± 0.09	12.66 ± 0.04	12.10 ± 0.05	0.681	0.494	-21.61 ± 0.12	-21.92 ± 0.12
15531	34.38 ± 0.06	13.85 ± 0.04	13.32 ± 0.05	0.223	0.162	-20.97 ± 0.08	-21.38 ± 0.08
16274	35.41 ± 0.04	13.67 ± 0.04	12.92 ± 0.05	0.199	0.144	-22.16 ± 0.06	-22.79 ± 0.07
19767	34.32 ± 0.06	14.06 ± 0.04	13.39 ± 0.05	0.135	0.098	-20.61 ± 0.08	-21.18 ± 0.08
20938	34.08 ± 0.07	14.25 ± 0.04	...	0.133	0.097	-20.18 ± 0.08	...
23333	34.05 ± 0.07	13.55 ± 0.05	...	0.085	0.062	-20.80 ± 0.09	...
23598	35.11 ± 0.04	13.67 ± 0.04	13.07 ± 0.04	0.160	0.116	-21.82 ± 0.06	-22.31 ± 0.06
23913	34.77 ± 0.05	13.71 ± 0.05	13.31 ± 0.05	0.185	0.134	-21.46 ± 0.07	-21.75 ± 0.07
24788	35.12 ± 0.04	13.59 ± 0.04	13.11 ± 0.05	0.091	0.066	-21.84 ± 0.06	-22.23 ± 0.07
26140	35.43 ± 0.04	12.74 ± 0.04	12.28 ± 0.05	0.085	0.061	-22.99 ± 0.06	-23.37 ± 0.06
26517	33.76 ± 0.08	14.54 ± 0.02	14.18 ± 0.02	0.126	0.092	-19.57 ± 0.08	-19.83 ± 0.08
27792	31.73 ± 0.20	0.049	0.036
28310	34.56 ± 0.05	...	13.86 ± 0.05	0.110	0.080	...	-20.94 ± 0.08
28401	33.47 ± 0.09	13.12 ± 0.05	12.42 ± 0.05	0.441	0.320	-21.01 ± 0.11	-21.53 ± 0.11
31159	34.52 ± 0.06	...	13.00 ± 0.05	0.104	0.075	...	-21.75 ± 0.08
32091	32.63 ± 0.13	0.090	0.065
32638	34.77 ± 0.05	13.11 ± 0.04	12.57 ± 0.04	0.062	0.045	-21.94 ± 0.07	-22.40 ± 0.07
33465	34.81 ± 0.05	12.51 ± 0.04	...	0.021	0.015	-22.54 ± 0.07	...
36925	34.94 ± 0.05	13.26 ± 0.10	12.61 ± 0.05	0.163	0.118	-22.06 ± 0.11	-22.60 ± 0.07
38268	33.28 ± 0.10	13.51 ± 0.02	13.03 ± 0.02	0.049	0.036	-20.04 ± 0.10	-20.44 ± 0.10
38908	34.99 ± 0.04	13.28 ± 0.05	13.00 ± 0.05	0.082	0.059	-22.01 ± 0.07	-22.20 ± 0.07
39728	32.64 ± 0.13	12.46 ± 0.04	...	0.056	0.041	-20.46 ± 0.14	...
46767	35.34 ± 0.04	12.56 ± 0.10	12.15 ± 0.05	0.035	0.026	-23.03 ± 0.11	-23.37 ± 0.06
49906	34.91 ± 0.05	13.88 ± 0.10	13.36 ± 0.05	0.084	0.061	-21.33 ± 0.11	-21.77 ± 0.07
55750	34.05 ± 0.07	13.58 ± 0.10	12.41 ± 0.05	0.165	0.120	-20.85 ± 0.12	-21.92 ± 0.09
56010	34.05 ± 0.07	15.30 ± 0.10	13.74 ± 0.05	0.085	0.061	-19.05 ± 0.12	-20.53 ± 0.09
57931	35.58 ± 0.03	13.86 ± 0.04	13.69 ± 0.05	0.029	0.021	-21.97 ± 0.06	-22.07 ± 0.06
58410	35.53 ± 0.04	13.54 ± 0.10	13.49 ± 0.05	0.033	0.024	-22.24 ± 0.11	-22.22 ± 0.06
70962	33.95 ± 0.07	13.16 ± 0.02	12.59 ± 0.02	0.123	0.089	-21.13 ± 0.08	-21.60 ± 0.08
71106	35.62 ± 0.03	12.78 ± 0.02	12.16 ± 0.02	0.208	0.151	-23.27 ± 0.05	-23.77 ± 0.04
72144	35.82 ± 0.03	14.80 ± 0.02	14.12 ± 0.02	0.168	0.122	-21.41 ± 0.04	-21.98 ± 0.04
72453	35.69 ± 0.03	13.74 ± 0.02	13.10 ± 0.02	0.187	0.135	-22.36 ± 0.05	-22.88 ± 0.04

The information provided here completes the description of the data sets for these previous studies. We have focused on R and I bands to (1) overlap the spectral region of our kinematic data and (2) to minimize disk structure and scatter in the TF relation due to star formation and extinction. While longer-wavelength data would be beneficial in the latter regard, the costs in observing time and signal to noise outweigh the gains at this stage in the analysis.

R -band and I -band images were acquired for the sample over 17 nights (10 runs) from 1999 May to 2001 January on (1) the 2.1 m telescope at KPNO (3 nights; 1 run); (2) the Harlan J. Smith 2.7 m at McDonald Observatory (3 nights; 1 run); and (3) the WIYN 3.6 m telescope at KPNO (11 nights; 8 runs) as part of a backup program that required excellent seeing and dark time. We used Harris filters, which provide colors that closely match the Kron–Cousins photometric system (Cousins 1978). The Appendix provides a detailed tabular summary of all observations, the quality of the photometric calibration, and our method for determining total magnitudes. Table 1 encapsulates the total apparent and absolute magnitudes in the R and I bands based on our photometric observations. These are used

in Section 5.2 to derive inclinations based on inverting the TF relations.

We calculated surface brightness profiles for our sample using the IRAF *ellipse* routine. *Ellipse* calculated isophotes in rings which had changing position angles and ellipticity. While the rings tend to follow spiral structure, surface brightness profiles derived using circular apertures were virtually indistinguishable because our galaxies are nearly face-on. We use these profiles in Section 3.2 to check the centering of our kinematic data.

We also used the disk surface brightness profiles to measure the disk concentration index. The concentration index $C \equiv 5 \log(r_{80\%}/r_{20\%})$, where the radii $r_{80\%}$ and $r_{20\%}$ enclose 80% and 20% of the light, respectively. Exponential profiles yield $C = 2.7$ and $r^{1/4}$ profiles have $C = 5.2$. Concentration indices for our sample were in the range $2.3 < C < 3.9$. We report the I -band concentration indices (unless the R -band image quality was far superior) in Table 2. Both R - and I -band images yielded nearly identical measures of the concentration index, consistent with the findings of Bershady et al. (2000) who showed that color systematics were negligible between B - and R -band measures of C .

Table 2
Photometric Structural Parameters

PGC	C	μ_0 (mag arcsec $^{-2}$)	h_R (arcsec)	r_{inner} (arcsec)	r_{outer} (arcsec)	b/a (I band)
2162	3.92	19.66	4.6 ± 0.2
3512	2.78	19.34	6.3 ± 0.2	25	30	0.93 ± 0.04
5673	2.76	20.52	11.5 ± 0.2	43	50	0.90 ± 0.01
6855	2.42	21.06	12.8 ± 0.2	40	48	0.89 ± 0.03
7826	2.63	20.39	9.8 ± 0.2
8941	2.91	19.92	8.1 ± 0.2	26	34	0.97 ± 0.02
14564	2.84	19.07	7.1 ± 0.2
15531	2.66	20.82	10.7 ± 0.2	33	44	0.84 ± 0.03
16274	2.80	20.21	8.8 ± 0.2	26	34	0.89 ± 0.02
19767	2.63	20.85	9.5 ± 0.2	30	38	0.86 ± 0.03
20938	3.89	19.03	5.0 ± 0.2
23333	2.68	20.95	8.4 ± 0.2	22	26	0.93 ± 0.02
23598	2.92	20.63	9.0 ± 0.2	32	38	0.91 ± 0.03
24788	2.94	19.54	5.4 ± 0.2
26140	3.58	19.55	8.2 ± 0.2	34	42	0.80 ± 0.01
26517	3.36	22.40
27792	2.66	...	9.5 ± 0.2	30	40	0.79 ± 0.02
28310	2.78	21.48	9.4 ± 0.2	31	38	0.91 ± 0.04
28401	2.67	20.66	16.0 ± 0.2	44	50	0.82 ± 0.02
31159	2.77	...	10.0 ± 0.2	38	43	0.83 ± 0.05
32091	2.63	...	13.6 ± 0.2	38	50	0.90 ± 0.03
32638	3.30	19.77	6.6 ± 0.2	14	23	0.92 ± 0.02
33465	3.22	20.36	10.2 ± 0.2	20	26	0.95 ± 0.02
36925	3.04	19.58	6.8 ± 0.2	19	24	0.93 ± 0.01
38268	2.90	21.22	...	35	46	0.73 ± 0.03
38908	3.10	19.46	5.6 ± 0.2	27	40	0.91 ± 0.04
39728	2.45	20.56	...	30	40	0.88 ± 0.01
46767	3.10	19.34	7.8 ± 0.2	44	51	0.87 ± 0.01
49906	2.72	20.26	7.1 ± 0.2	30	32	0.94 ± 0.01
55750	2.37	20.28	12.7 ± 0.2	38	47	0.94 ± 0.02
56010	2.74	21.22	9.0 ± 0.2
57931	3.49	21.03	8.5 ± 0.2	24	31	0.89 ± 0.04
58410	3.08	19.88	8.7 ± 0.2	40	50	0.86 ± 0.03
71106	3.52	18.89	5.6 ± 0.2	30	36	0.87 ± 0.04
72144	3.60	21.10	6.8 ± 0.2	20	27	0.91 ± 0.05
72453	3.14	20.60	9.4 ± 0.2

2.3. Velocity-field Maps

Since the geometry of the DensePak array was regular (with the exception of five broken fibers), producing rudimentary velocity fields using the Gaussian centroids was straightforward. To produce smooth velocity-field maps, however, required the use of interpolation schemes. We used the *griddata* function in IDL, which interpolates between scattered data values on a plane. We used an inverse distance algorithm, considering only values with a 5 arcsec radius of a given point in the plane and a smoothing radius of 2.5 arcsec. These smoothed velocity fields are useful for qualitative comparisons of, e.g., the spiral arm pattern in images and “kinks” in the iso-velocity contours, but we emphasize that only the discrete observed velocities are used when performing any quantitative analysis such as velocity-field fitting or measuring rotation-curve asymmetries.

By comparing each DensePak fiber’s observed velocity centroid and the mean velocities calculated in the fiber footprint of the smoothed velocity-field maps, we ascertained that the smoothed velocity-field maps created via the inverse distance interpolation algorithm yielded good representations of the velocity fields. We found that the standard deviation between the observed velocities and the velocities obtained from the smoothed velocity field differed by 5% of the total peak to val-

ley of observed velocities (typically 8 km s $^{-1}$). Most of the difference is observed near the center where the velocity-field gradient is greatest. Velocity fields for all 39 galaxies are presented in Figure 1. Each velocity field is derived from two or three independent positionings, or pointings of the DensePak IFU on the galaxy, as described in Andersen et al. (2006). In this figure, we register the different DensePak pointings based on our velocity-field modeling described in Section 3.1.

2.4. H α Flux Maps

Using the same interpolation algorithm described above, we also created H α flux maps of the galaxies (at least for that area of the galaxy covered by the DensePak footprint), shown in Figure 2. Inspection of these images enables us to assess the extent to which the patchy nature of H α emission (e.g., Figure 14 from Paper II) may unduly bias our velocity-field maps to specific radial zones or discrete azimuthal regions. We see a wide diversity of H α flux distributions. Some galaxies show H α emission clearly following the spiral arm structure (e.g., PGC 2162, PGC 16274, and PGC 26140), some galaxies show a paucity of emission at the center (e.g., PGC 15531, PGC 19767, and PGC 38268), some show a central concentration of H α (e.g., PGC 24788, PGC 32638, and PGC 57931),

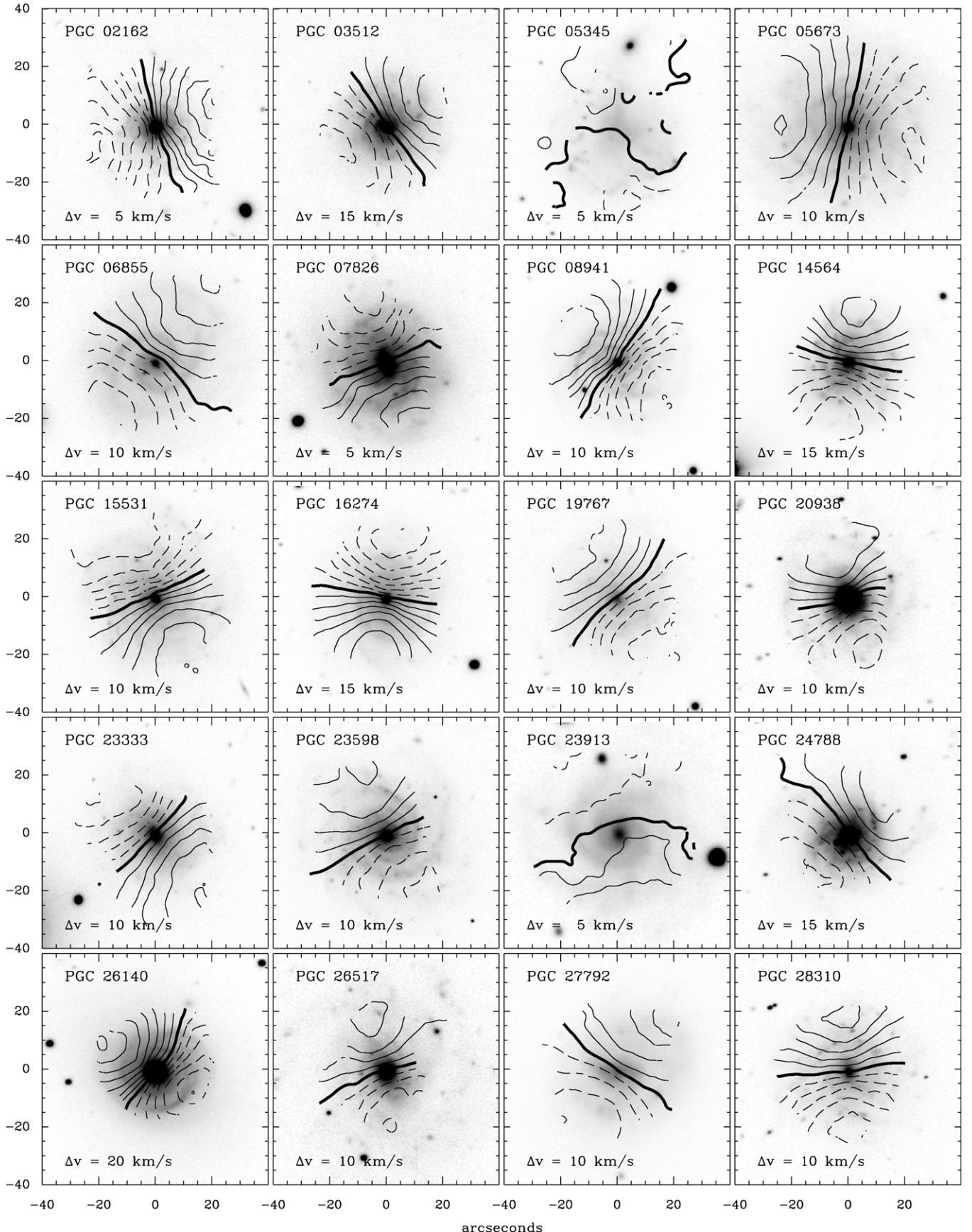
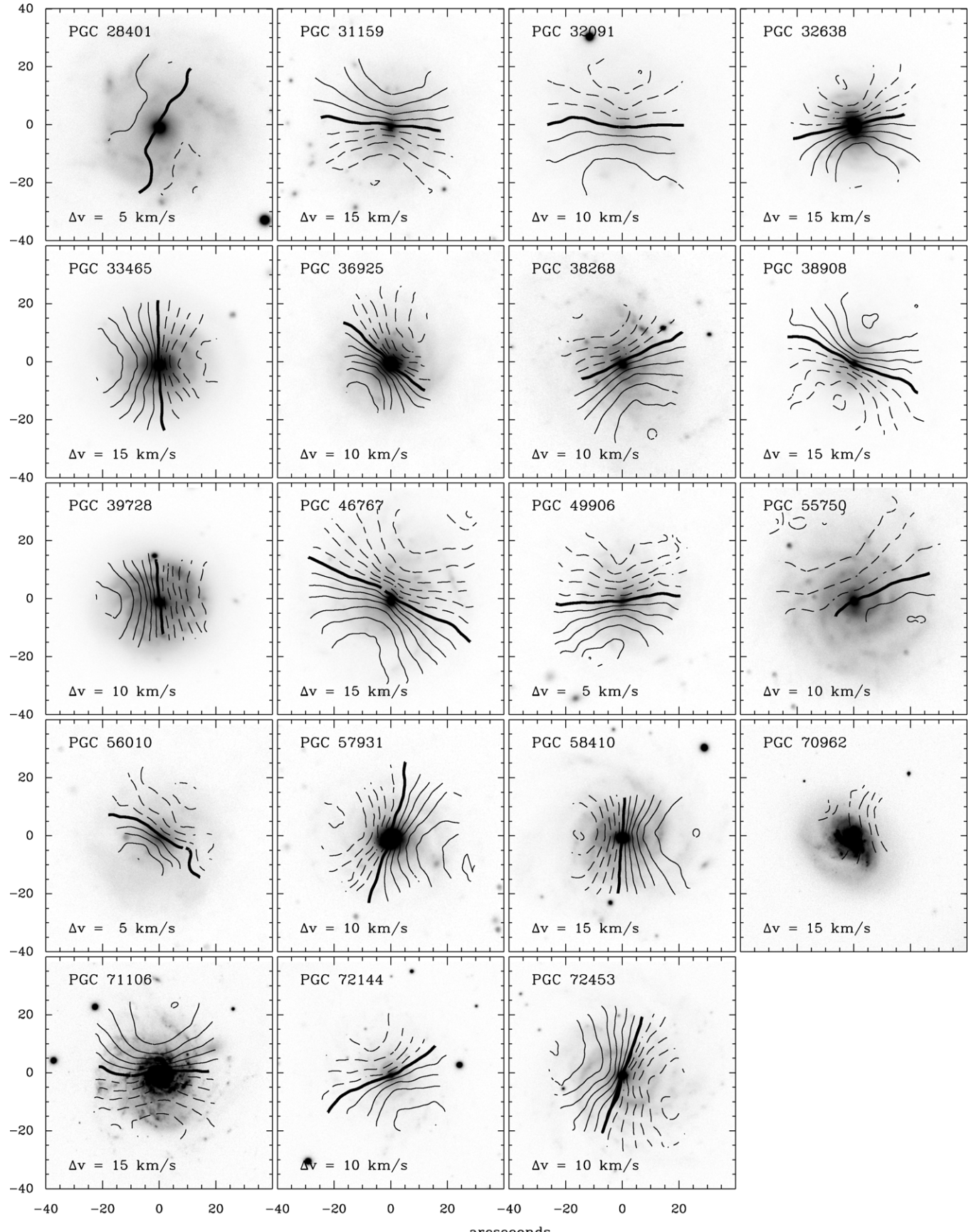


Figure 1. Velocity fields for the sample galaxies from our survey. The minor axis iso-velocity contour is marked with a thick solid line. Solid lines are iso-velocity contours which are receding with respect to the systematic velocity, while dashed lines mark approaching iso-velocity contours. The velocity spacing between contours is shown in the bottom left of each panel. Even galaxies such as PGC 23598 with observed rotation velocities less than 50 km s^{-1} have well-defined major and minor axes.

**Figure 1.** (Continued)

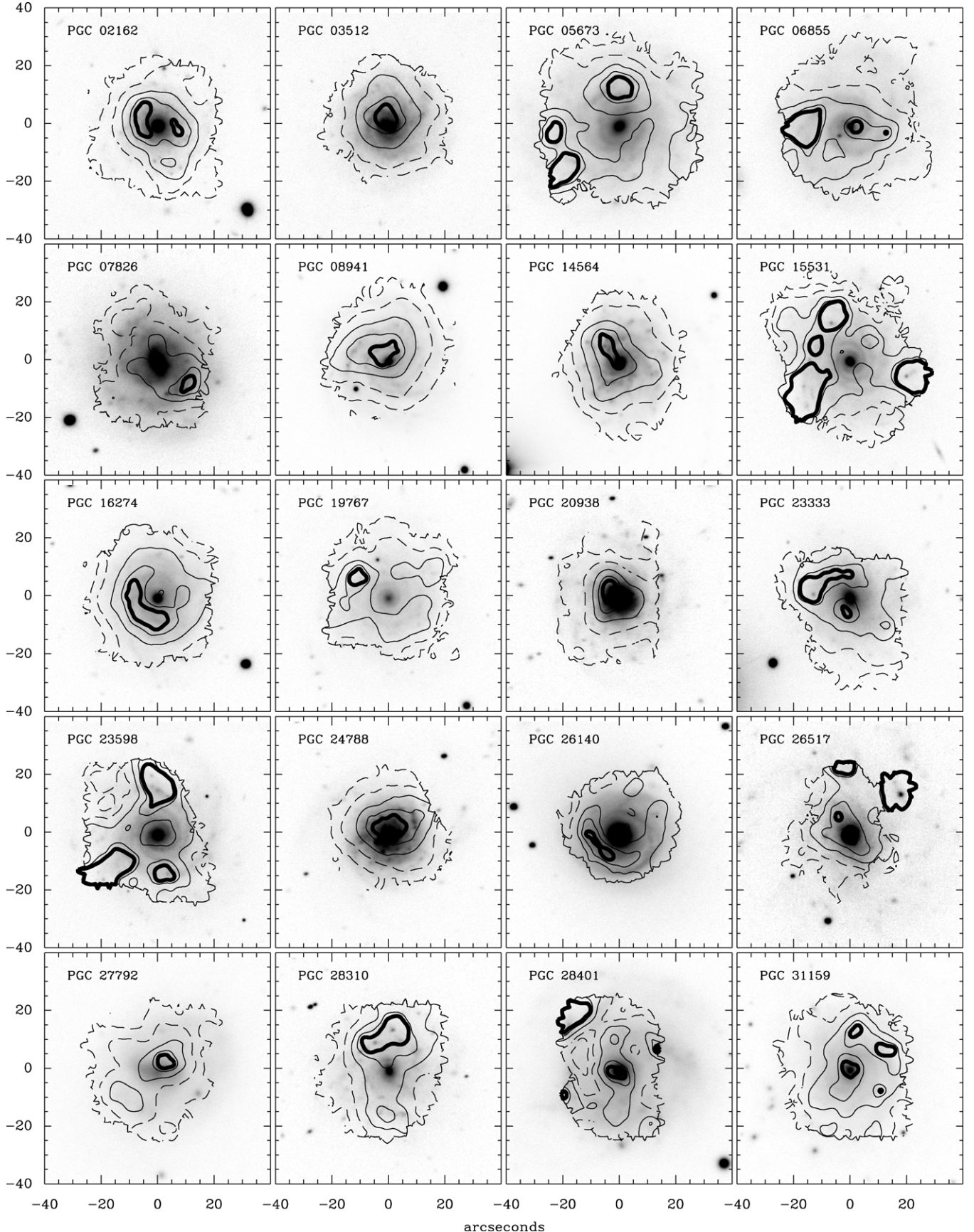


Figure 2. H α flux maps for the 36 sample galaxies with velocity-field model fits overlayed on broadband R-band (or I band of R is unavailable) images. Contours are based on the minimum and maximum fluxes in the maps. Based on this range, contours mark the 10%, 25% (both marked with dashed lines), 50%, 75%, and 90% (heavy solid line) iso-flux levels.

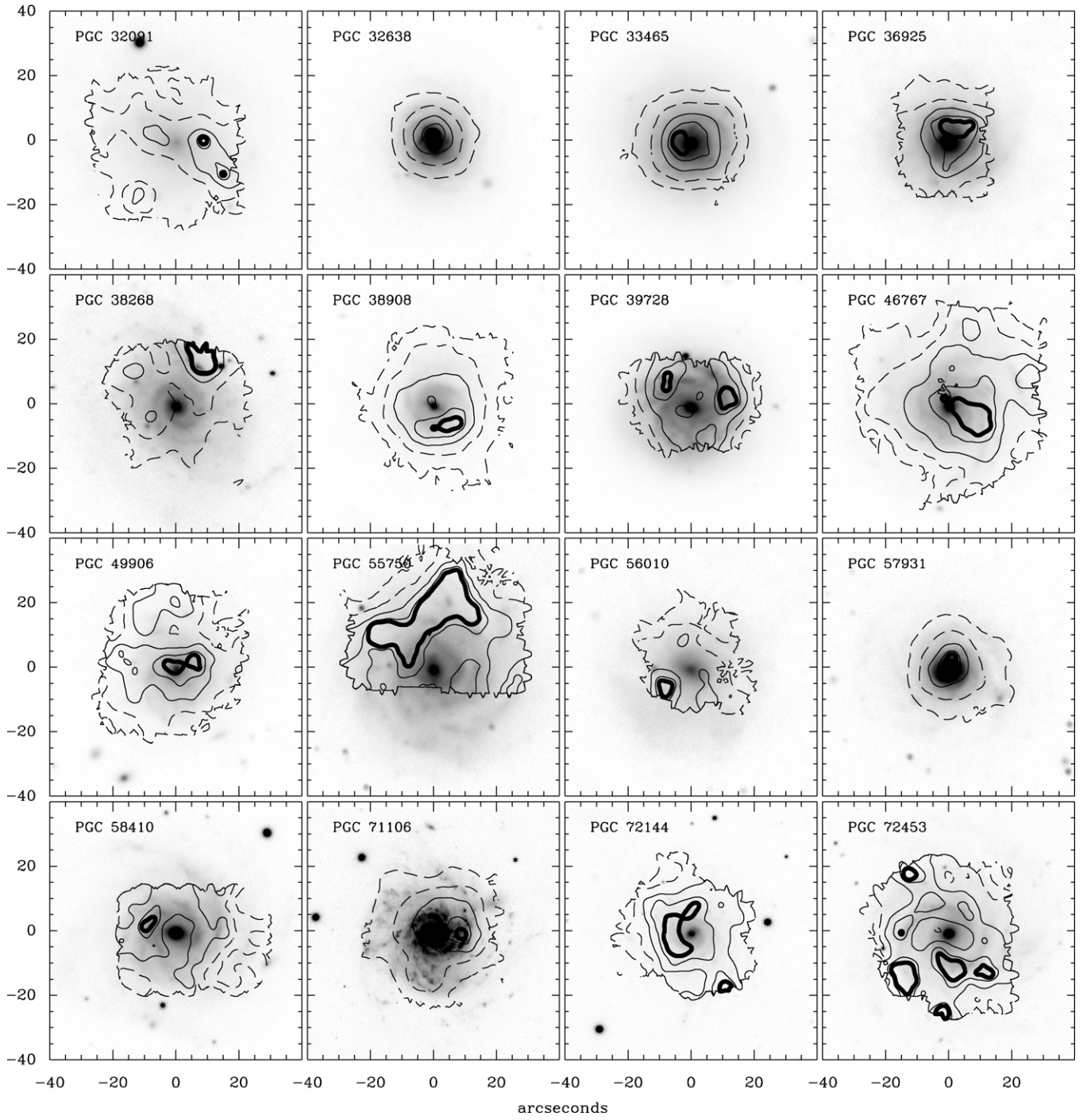


Figure 2. (Continued)

many show an H α flux concentration near but offset from the photometric center (PGC 3512, PGC 8941, PGC 14564, and PGC 33465), and many show peaks in emission coincident with point-like objects in the broadband images which presumably are H II regions (e.g., PGC 26517, PGC 28310, and PGC 38268).

A common characteristic of these flux maps, however, is the sensitivity of DensePak to low levels of H α flux, i.e., diffuse emission. If we compare the DensePak H α flux maps with the MOSCA H α images presented in Paper II (Figure 3), we see that the DensePak maps closely mirror the higher spatial resolution MOSCA H α images, but go deeper: H α is detected throughout

the disk. The greater depth is due to a combination of large spaxels, long effective exposures per resolution element (about a factor of 10 longer than typical Fabry–Perot observations of comparable spectral resolution; e.g., Garrido et al. 2002), and high spectral resolution (about a factor of 230 higher than our narrowband imaging) which minimizes shot noise from sky foreground and source continuum. As such, DensePak H α observations provide relatively uniform and complete spatial maps of the galaxies' kinematics. Individual velocity measurements (i.e., measurements from one fiber spectrum), are of course influenced by the distribution of flux within a fiber. This effect could introduce random errors in our velocity asymmetry

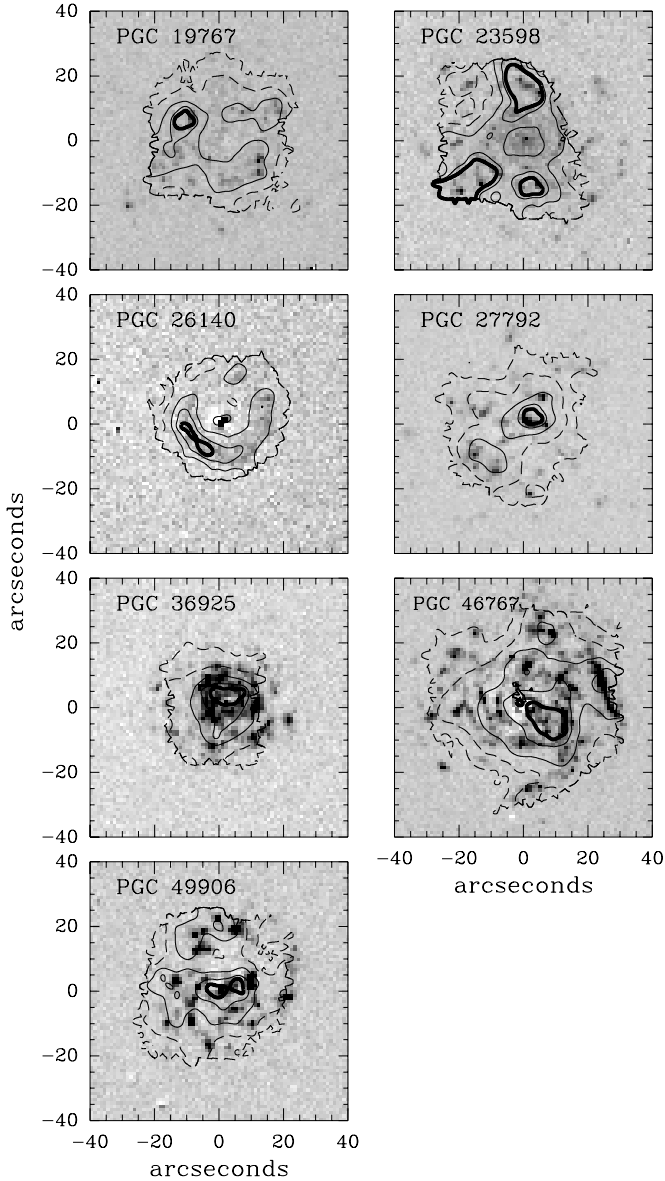


Figure 3. H α flux maps for seven galaxies overlaid on H α imaging from MOSCA on the Calar Alto 3.5 m telescope. Contours are based on the minimum and maximum fluxes in the maps. Based on this range, contours mark the 10%, 25% (both marked with dashed lines), 50%, 75%, and 90% (heavy solid line) iso-flux levels. The correspondence between the DensePak H α contours and the H α imaging is very good. In some cases, the DensePak footprint does not cover all the H α emission from the galaxy (e.g., the emission west of the center of PGC 23598), but note also that H α DensePak flux is detected in regions of the galaxy where no emission is apparent from the MOSCA images.

measurements, but the overall kinematics of the galaxy are well sampled by the H α emission detected in the DensePak data.

3. MODELING VELOCITY FIELDS

The process of fitting tilted rings to galaxy velocity fields (e.g., Begeman 1989; Verheijen & Sancisi 2001; Swaters et al. 2003; Kirby et al. 2012) is a powerful and widely used tool for measuring the geometry and rotation speed of atomic gas in disk galaxies. However, as we noted in the Introduction, H α velocity fields are distinct from their H 1 counterparts in two important respects. First, H 1 maps extend far out in galaxies, beyond the optical disk, and are often subject to warps and other asymmetries, while H α rotation curves typically extend

to roughly three scale lengths (Christlein et al. 2010) and are therefore not subject to warps in most normal galaxies (Saha et al. 2009). Therefore, H α velocity fields of normal spiral galaxies often can be described with a single geometry (position angle ϕ_0 and inclination i) except when there are bars, strong asymmetries, or solid body rotation (the galaxies in this sample were chosen to be photometrically regular and to not contain strong bars). The second difference between H 1 and H α velocity fields is again related to the radial extent of the data; the majority of H 1 disk galaxy velocity fields lie beyond the steeply rising part of the rotation curve, while the fraction of the H α velocity fields affected by the rising part of the rotation curve is often substantial. Tilted-ring fits to the inner regions that are wide enough to contain a sufficient number of velocity measurements still will be poorly constrained. This is because the rotation speed within the ring is modeled to be constant in radius, while what is observed has a spread in velocities due to the radial gradient across the ring; residuals between model and data cannot be removed even if the correct geometry for the ring is used. If instead a radial rotation-curve model is assumed, one can use data even on the steeply rising part of the rotation curve to constrain the disk geometry.

For these reasons, we have explored the capability of a single, inclined, differentially rotating, circular disk model to fit adequately the DensePak H α velocity fields. The velocity-field modeling we undertake is two-dimensional (2D), simultaneously minimizing the projected velocity trends in azimuth and radius with respect to a model rotation curve.

The primary distinction between our method, and the more traditional tilted-ring fitting method is that we adopt one geometric zone, and fit a rotation curve to the 2D kinematic data. Ring fitting enables multiple geometric zones, but the one-dimensional treatment of the kinematic data takes no advantage of information about the rotation curve and hence the covariance between radius and azimuth in an inclined system. The primary advantage of using a 2D approach over using tilted rings comes at low inclination. At low inclination tilted-ring fits tend to diverge unless the fit is weighted by $|\cos \theta|$ (θ is the angle between the galaxy's major axis in the galaxy plane) and data with $|\theta| < \theta_{\max} = 45^\circ$ are typically removed from the fit to minimize the effects of warping on tilted-ring fits (Begeman 1989; Verheijen & Sancisi 2001). However, the greatest differences between two velocity-field models with slightly different inclinations occur at $\theta > 45^\circ$ (van der Kruit & Allen 1978; Epinat et al. 2008), precisely where tilted-ring fits often do not consider the data (Figure 4). Nearly face-on galaxies show the smallest differences between velocity fields with slightly different inclinations, so it is imperative to use data at all azimuthal angles to accurately fit velocity-field models at inclinations less than 30° . With our 2D approach, it is not necessary to down-weight or exclude particular azimuthal regions so we are able to maximize the signal from the kinematic data which constrains inclination.

A secondary but significant advantage with a 2D approach comes from adopting a rotation curve. In addition to leveraging the covariance between radius and azimuth, a single velocity-field model can use the entire data set to constrain the fit even in the presence of radial velocity gradients (e.g., a non-flat rotation curve). Since we typically have ~ 150 fibers with H α emission for a survey galaxy, we prefer to use all data to constrain inclination, position angle, and other fit parameters, rather than breaking the galaxy into three or more rings with fewer than 50 measured velocity centroids per ring.

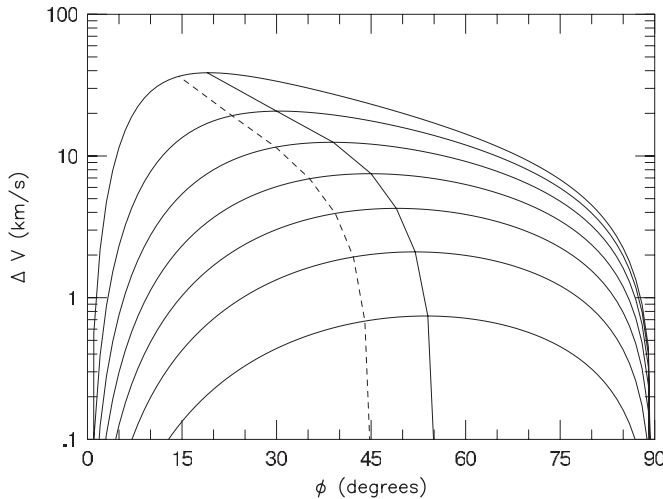


Figure 4. Differences in velocity as a function of ϕ , where ϕ is measured from the major axis in the *observer's frame*, assuming (1) measurements are made on the flat part of the rotation curve, (2) $v_{\text{rot}} = 160 \sin i \text{ km s}^{-1}$ for the mean inclination, and (3) velocity fields obey Equations (1)–(4). From the bottom: solid curves represent mean inclinations of $15^\circ, 25^\circ, 35^\circ, 45^\circ, 55^\circ, 65^\circ$, and 75° with inclination differences of $\pm 5^\circ$. The dashed line represents $\theta = 45^\circ$ for each of these different inclinations, where θ is the angle from the major axis in the *galaxy plane*. The solid line represents the maximum velocity difference as a function of ϕ for different inclinations. Classical tilted-ring fits typically do not utilize data to right of dashed line (e.g., Begeman 1989), thereby missing over half the signal used to estimate inclination.

The simplest velocity-field model involves the assumption that the rotation curve of a galaxy is radially symmetric and the velocity field is axisymmetric. An expression for the velocity at any point in the galaxy plane (using the notation of van der Kruit & Allen 1978), $V_{\text{obs}}(R, \theta)$, where R and θ are the radius and azimuthal angle in the galaxy plane, is given by

$$V_{\text{obs}}(R, \theta) = V_{\text{sys}} + V_\theta(R) \sin i \cos \theta, \quad (1)$$

where V_{sys} is the systematic recession velocity, and $V_\theta(R)$ is the *intrinsic* (i.e., already corrected for inclination) rotation speed. For convenience, we define $v_\theta(R) \equiv V_\theta(R) \sin i$ to be the *observed* rotation speed, where i is the inclination. Relations between these quantities and an observed radius and azimuthal angle, r and ϕ , are given by

$$R = r \cos(\phi - \phi_0) \cos \theta \quad (2)$$

and

$$\tan \theta = \tan(\phi - \phi_0) \cos i, \quad (3)$$

where ϕ_0 is the position angle.

To be able to model the kinematics of the whole disk, we need to assume a functional form for the galaxy rotation curve [$v_\theta(R)$]. Several universal rotation-curve models exist in the literature (e.g., Persic & Salucci 1991; Courteau 1997), but we made another simplifying assumption after examining the tangential speeds for circular orbits on the major axis (i.e., rotation curves) of the sample galaxies. The rotation curves all showed a steady rise to a peak velocity. Thus, the rotation curve required only two free parameters—the peak velocity and a characteristic scale length, h_{rot} . A single inclined hyperbolic tangent rotation curve

$$v_{\theta, \text{tanh}}(R) = v_{\text{rot}} \tanh(R/h_{\text{rot}}) \quad (4)$$

was sufficient to fit the shape of these rotation curves with a minimum of free parameters. Note that v_{rot} is the *projected*

asymptotic velocity, i.e., uncorrected for inclination. Though hyperbolic tangent models for rotation curves are not directly motivated by a physical model, the pseudo-isothermal sphere parameterization of dark halo density profiles yields an arctangent model for the rotation curve (Gilmore et al. 1990; de Blok & McGaugh 1997; Swaters et al. 2003; Puech et al. 2008):

$$v_{\theta, \text{pISO}}(R) = \sqrt{4\pi G \rho_0 r_c^2 \left[1 - \frac{r_c}{r} \arctan\left(\frac{r}{r_c}\right) \right]} \sin i. \quad (5)$$

We define the asymptotic rotation speed for this pseudo-isothermal model to be $v_{\text{pISO}} \equiv \sqrt{4\pi G \rho_0 r_c^2} \sin i$. Section 4.1 shows that the pseudo-isothermal model yields decent fits to the rotation curves, but in Section 5.3 we show that the asymptotic velocities derived from the pseudo-isothermal fits are not as indicative of the flat rotation speed as is v_{rot} derived from the tanh model.

In our modeling, the free variables are inclination, position angle, center, central velocity, observed rotation velocity, and scale length. Our method, however, is easily generalizable to more complicated rotation-curve forms. All fits include heliocentric corrections.

3.1. χ^2 Minimization of Velocity-field Models

We found a best-fit velocity-field model to each galaxy's observed kinematic data from DensePak using nonlinear χ^2 minimization. We generated a smooth model using Equations (1)–(4) with the seven free parameters listed above plus two free parameters corresponding to telescope offsets for each additional DensePak pointing.

One effect we had to account for in our fitting code is “beam smearing.” An IFU fiber is like a radio “beam”; both smooth or “smear” signal velocities within a given radius. We map the model over the region spanned by the observations on a grid with a scale of four “pixels” per arcsecond (~ 110 model pixels per fiber). The spatial resolution of this beam-smearing correction was important: χ^2 calculated for a given set of free parameters changed on the order of 10% if sampled with fewer than four pixels per arcsecond (~ 12 pixels per fiber diameter) and remained relatively constant at higher spatial resolutions. This beam-smearing model includes the assumption that the H α flux is distributed uniformly across each DensePak fiber. This is certainly not true in all cases, but without H α imaging of the full sample, it is difficult to more realistically model beam smearing. Since we do not know the distribution of H α , we also do not account for the seeing during the observation. However, the effect of seeing on our data should be small as the seeing during our DensePak observations was usually an arcsecond or better, significantly less than the 3'' DensePak fiber. Our beam-smearing correction is then obtained by determining the mean, $V_{\text{mod},i}$, and standard deviation, $\sigma_{\text{beam},i}$, of the velocity of the smoothed model within the i th DensePak fiber footprint. The beam-smearing correction, $\sigma_{\text{beam},i}$, is added in quadrature to the centroid fitting error and has its largest magnitude in those fibers in which the derivative of the model velocity is greatest. This beam-smearing term accounts for the unknown spatial distribution of H α within the DensePak fibers. The mean beam-smearing error is typically 4% of v_{rot} , with a maximum of $\sim 20 \text{ km s}^{-1}$ for the central fibers of PGC 26140, which has the correspondingly largest derived v_{rot} .

Since χ^2 is computed from a convolution of the DensePak footprint with the model velocity field, we use a nonlinear

method of minimizing χ^2 over the multidimensional space of the free parameters. We adopted a modified multidimensional downhill simplex method that incorporates simulated annealing (Press et al. 1992) for finding the minimum of χ^2 . While this algorithm is not computationally efficient, it is effective at finding the minimum in a potentially topologically complicated χ^2 space. The Metropolis (Metropolis et al. 1953; Simard 1998) algorithm that we adopt uses a “temperature” to add a log-normally distributed set of random values to the current best solution; the higher the temperature, the larger the random errors. Operating from this initial guess, the algorithm steps through multidimensional space toward the direction which corresponds to the greatest decrease of the function χ^2 by using a downhill simplex. Once the fit has converged (to a perhaps local minimum), the temperature is reduced and the procedure is repeated. Every five times this procedure is repeated, the very best solution is used to restart the algorithm. This helps prevent the algorithm from staying in a local minimum.

While the Metropolis algorithm is a powerful tool for finding the minimum of a large multi-variable nonlinear equation, we found that if the solution were arrived at in steps, the algorithm would find the minimum more efficiently. When initially fitting a galaxy velocity field, several parameters were kept fixed. We initially fixed the inclination to 30° , $h_{\text{rot}} = 5$ arcsec, and fixed the center and pointing offsets based on the telescope offsets. After we held these parameters fixed, the Metropolis algorithm minimized χ^2 by varying the remaining parameters (i.e., position angle, rotation speed, and systemic velocity). After this initial fit was determined, we allowed the center to vary. Finally, we freed the remaining parameters and re-fit the velocity field. After arriving at an initial solution, we perturbed this solution by varying both the initial conditions and step sizes to ensure we had found the true χ^2 minimum and not just a local minimum. We continued perturbing the Metropolis solutions until differences in inclination and position angles were less than <0.1 . Similarly, all velocity solutions and position solutions were required to be stable to <0.1 km s $^{-1}$ or arcseconds, respectively.

Although the velocity-field residuals were small, typically less than 6 km s $^{-1}$, our velocity centroiding errors were ~ 2 km s $^{-1}$ (Andersen et al. 2006), resulting in minimum reduced- χ^2 , χ^2_v , for these fits which were typically much greater than unity ($2 < \chi^2_v < 15$). For any χ^2 fit where χ^2_v is much greater than unity there are several possible explanations: (1) error bars on the line centroids are underestimated, (2) the residuals of our velocity-field model fit are not Gaussian, or (3) the model is not a good representation of the data. Based on our analysis of the H α emission line data in Paper I, we believe our line centroid measurements are reasonable and that the errors are not grossly underestimated. The other two explanations are related. Indeed, one would not expect our simple model to approximate the true velocity field because in detail the velocity fields of real galaxies are very complicated. This mismatch between reality and our velocity-field model will give rise to residuals that are non-Gaussian. Since the spectral resolution of our DensePak observations is relatively high, it is reasonable to suppose we are seeing the true complexities of disk kinematics. Presumably, a class of models exists which would better match the data. Such models would need to possess high spatial frequencies composed to match all the fluctuations in the observed velocity fields. Some of these components may be random in nature, so such a complex model would need to be statistical. Further, since we are not interested here in modeling

the random motions of H α regions and the non-random, but high spatial frequency streaming associated with spiral arms, we treat all such variations as having random spatial distribution. (We address the suitability of this treatment in Section 4.4.) We then compensate for these contributions by adding a “fuzziness” term to our model. Specifically, we follow the probability theory arguments of Rix et al. (1997) by adding an extra error term, σ_{mod} , into the χ^2 sum:

$$\chi^2_\delta = \sum_i \frac{(V_{\text{mod},i} - V_{\text{obs},i})^2}{\sigma_{\text{mod}}^2 + \sigma_{\text{obs},i}^2 + \sigma_{\text{beam},i}^2}. \quad (6)$$

For each galaxy, we chose a value for σ_{mod} which normalized the reduced- χ^2_δ to unity based on an initial fit using the standard χ^2 definition. We then re-fit the galaxy velocity field to find a new minimum-valued solution using Equation (5). We adjusted σ_{mod} to lower values as needed to keep χ^2 within 1% of the difference between the number of observed velocities and the degrees of freedom.

Table 3 contains velocity-field fits for all the sample galaxies along with the added noise term σ_{mod} . We note that σ_{mod} is less than 6 km s $^{-1}$ for all galaxies except PGC 38908 and PGC 71106. Using this fitting method, we were able to fit velocity fields to 36 of 39 galaxies (a 90% success rate). The inclination values presented in Table 3 differ slightly from the kinematic inclinations presented in Andersen & Bershady (2003), but the results are consistent within the errors. The differences are due to improved measurements of the line centroids (Andersen et al. 2006) and changes in the velocity-field fitting algorithm (the earlier results did use the more robust Metropolis algorithm described in Section 3.1). The three galaxies for which we could not fit velocity-field models included:

PGC 05345. It is a Magellanic Irregular that has limited H α scattered in separated regions. The small amount of H α in the galaxy is all at the same velocity ($\sigma_{\text{rms}} = 2.5$ km s $^{-1}$). These two factors added together prevent the fitting algorithm from converging.

PGC 23913. It also has a very small velocity gradient ($v_{\text{rot}} \sim 10$ km s $^{-1}$), which implies a very low inclination. The velocity gradient is so shallow, the fitting algorithm could not settle on a model center.

PGC 70962 (MRK 318). It is a star-bursting galaxy in which H α emission was detected in only 39 fibers. We expect that the number of velocities available are insufficient to be fit by the velocity-field model, even if the true velocity field in the center of this galaxy is indeed that of a rotating disk (which it does not appear to be).

3.2. Spectroscopic Continuum Profiles: A Check on Telescope Offsets

Before turning to a presentation of our velocity-field parameter error estimation, since ours is a multi-parameter model it is worthwhile to examine whether errors on parameters of little astrophysical interest can be marginalized. Here, we examine constraints on the relative spatial registration of the data so that we may focus in subsequent sections primarily on the parameters of inclination and projected rotation velocity.

Figure 5 presents sample radial profiles of measured continuum flux (i.e., surface brightness) from DensePak. In addition to demonstrating our ability to measure such profiles spectroscopically, these surface brightness profiles are important because they indicate that (1) our velocity-field model centers agree with

Table 3
H α Velocity-field Fits and Kinematic Asymmetries

PGC	σ_{mod} (km s $^{-1}$)	N	i (deg)	ϕ_0 (deg)	v_{rot} (km s $^{-1}$)	h_{rot} (arcsec)	V_{sys} (km s $^{-1}$)	A_{RC}	A_{ϕ}
02162	3.1	153	29.1 $^{+4.7}_{-6.4}$	284.2 \pm 0.6	36.7 \pm 0.4	3.5 \pm 0.4	5434.7 \pm 0.3	0.069	0.077
03512	2.0	133	31.1 $^{+2.3}_{-2.4}$	300.5 \pm 0.3	83.2 \pm 0.5	6.9 \pm 0.1	5431.3 \pm 0.2	0.031	0.034
05673	2.4	237	22.0 $^{+3.1}_{-3.9}$	78.0 \pm 0.4	58.3 \pm 0.2	9.0 \pm 0.2	4489.3 \pm 0.2	0.047	0.041
06855	3.6	196	43.6 $^{+2.3}_{-3.0}$	321.0 \pm 0.6	54.7 \pm 0.5	10.9 \pm 0.4	4839.6 \pm 0.3	0.180	0.057
07826	2.6	139	44.1 $^{+4.5}_{-4.7}$	204.6 \pm 0.8	33.3 \pm 0.4	11.8 \pm 0.3	2363.0 \pm 0.2	0.089	0.095
08941	2.7	146	0.3 $^{+9.9}_{-0.3}$	58.7 \pm 0.3	68.8 \pm 0.5	4.9 \pm 0.2	9449.5 \pm 0.3	0.033	0.042
14564	4.4	151	30.6 $^{+2.9}_{-3.2}$	347.6 \pm 0.4	92.3 \pm 0.5	6.1 \pm 0.2	3481.70 \pm 0.4	0.075	0.043
15531	3.2	189	0.6 $^{+8.9}_{-0.6}$	206.3 \pm 0.4	65.4 \pm 0.4	7.0 \pm 0.2	5559.8 \pm 0.3	0.035	0.050
16274	2.2	151	34.4 $^{+1.7}_{-1.7}$	169.3 \pm 0.4	115.9 \pm 0.6	6.8 \pm 0.2	8877.2 \pm 0.4	0.016	0.025
19767	1.9	143	3.1 $^{+9.2}_{-3.1}$	44.1 \pm 0.4	54.0 \pm 0.4	8.9 \pm 0.2	5134.2 \pm 0.2	0.046	0.049
20938	4.1	266	16.9 $^{+5.0}_{-8.7}$	20.3 \pm 0.5	58.4 \pm 0.5	4.6 \pm 0.3	4678.9 \pm 0.3	0.099	0.063
23333	2.1	132	28.6 $^{+3.2}_{-4.3}$	227.7 \pm 0.5	60.8 \pm 0.4	9.2 \pm 0.2	4643.1 \pm 0.2	0.032	0.045
23598	1.9	149	22.8 $^{+4.5}_{-6.4}$	31.2 \pm 0.4	46.3 \pm 0.2	6.4 \pm 0.2	7475.6 \pm 0.2	0.059	0.050
24788	5.6	123	38.2 $^{+4.9}_{-4.9}$	312.1 \pm 1.0	85.0 \pm 1.4	12.7 \pm 0.5	7555.7 \pm 0.7	0.103	0.071
26140	4.3	146	26.1 $^{+3.2}_{-2.8}$	58.6 \pm 0.4	152.8 \pm 1.2	5.1 \pm 0.3	8824.1 \pm 0.8	0.033	0.043
26517	3.8	113	7.0 $^{+15.5}_{-7.0}$	21.9 \pm 0.9	48.3 \pm 0.6	5.9 \pm 0.3	4138.8 \pm 0.4	0.055	0.078
27792	3.7	145	38.7 $^{+3.8}_{-5.1}$	324.4 \pm 0.8	48.4 \pm 0.5	10.6 \pm 0.4	1458.0 \pm 0.3	0.086	0.068
28310	2.5	141	37.1 $^{+2.7}_{-2.7}$	8.0 \pm 0.5	65.5 \pm 0.4	9.6 \pm 0.2	5904.1 \pm 0.3	0.035	0.043
28401	2.2	152	27.0 $^{+9.0}_{-27.0}$	65.5 \pm 2.6	9.3 \pm 0.4	9.1 \pm 1.4	3351.8 \pm 0.2	0.209	0.255
31159	2.1	157	24.0 $^{+2.8}_{-3.0}$	-7.7 \pm 0.4	86.4 \pm 0.4	7.9 \pm 0.2	5785.3 \pm 0.3	0.029	0.030
32091	4.0	157	1.2 $^{+15.4}_{-1.2}$	178.2 \pm 0.8	42.8 \pm 0.6	9.2 \pm 0.4	2509.3 \pm 0.4	0.178	0.073
32638	5.0	129	26.9 $^{+3.6}_{-4.8}$	192.8 \pm 0.4	87.4 \pm 0.6	2.2 \pm 0.2	6502.9 \pm 0.4	0.003	0.041
33465	2.7	129	20.7 $^{+3.3}_{-4.7}$	92.1 \pm 0.3	100.8 \pm 0.6	3.7 \pm 0.2	6486.0 \pm 0.4	0.030	0.033
36925	2.1	76	23.7 $^{+3.8}_{-4.9}$	134.9 \pm 0.4	75.6 \pm 0.5	2.0 \pm 0.2	6823.1 \pm 0.4	0.059	0.034
38268	2.6	141	28.9 $^{+3.8}_{-4.1}$	206.5 \pm 0.5	64.8 \pm 0.5	8.5 \pm 0.2	3146.2 \pm 0.3	0.068	0.048
38908	6.5	157	32.0 $^{+3.5}_{-3.9}$	333.3 \pm 0.4	90.6 \pm 0.7	2.5 \pm 0.2	7087.8 \pm 0.5	0.055	0.057
39728	2.2	72	31.2 $^{+3.4}_{-4.1}$	97.1 \pm 0.4	76.4 \pm 0.5	7.7 \pm 0.2	2305.4 \pm 0.3	0.065	0.034
46767	4.7	229	23.3 $^{+2.5}_{-3.1}$	153.5 \pm 0.3	112.8 \pm 0.6	6.1 \pm 0.2	8302.0 \pm 0.4	0.023	0.037
49906	3.1	145	0.3 $^{+15.1}_{-0.3}$	182.7 \pm 0.9	31.0 \pm 0.4	8.2 \pm 0.4	6910.2 \pm 0.2	0.104	0.072
55750	2.8	151	10.6 $^{+9.4}_{-10.6}$	202.6 \pm 0.6	41.6 \pm 0.4	10.0 \pm 0.4	4529.3 \pm 0.2	0.093	0.059
56010	4.1	75	1.0 $^{+28.0}_{-1.0}$	143.4 \pm 1.3	26.1 \pm 0.8	6.0 \pm 0.7	4496.9 \pm 0.4	0.221	0.125
57931	3.3	127	20.7 $^{+4.5}_{-6.5}$	252.9 \pm 0.4	70.7 \pm 0.5	4.0 \pm 0.2	9265.4 \pm 0.4	0.047	0.046
58410	3.2	159	31.6 $^{+2.0}_{-2.1}$	267.5 \pm 0.3	113.0 \pm 0.5	5.1 \pm 0.2	9060.7 \pm 0.4	0.044	0.033
71106	9.5	159	14.0 $^{+9.0}_{-14.0}$	-0.9 \pm 0.7	97.6 \pm 0.9	7.3 \pm 0.3	9588.2 \pm 0.6	0.148	0.063
72144	2.7	110	24.4 $^{+5.2}_{-9.1}$	207.8 \pm 0.6	51.5 \pm 0.5	4.3 \pm 0.2	10509.5 \pm 0.3	0.064	0.061
72453	3.3	144	22.4 $^{+3.8}_{-5.0}$	71.9 \pm 0.4	77.3 \pm 0.6	5.0 \pm 0.3	9944.6 \pm 0.3	0.021	0.045

the photometric centers of the galaxies and (2) by letting telescope offsets vary during the model velocity-field fitting process we were able to improve the combination of DensePak pointings. In other words, after χ^2_{δ} minimization of the velocity-field models, where telescope offsets were free parameters, the surface brightness profile became tighter and were in good agreement with the R-band surface brightness profiles. Keep in mind that the velocity-field model fits rely on the emission-line (kinematic) data only; the tightness of the surface brightness profile is not coupled to the fit. Based on variations in model telescope offsets coupled with our observing experience, we find that errors in telescope offsets could be as great as 2 arcsec.

As an independent check of our “kinematic” centering, we matched the spectral continuum in the (Integral Field Spectroscopy (IFS)) data cubes, in a least-squares sense, with photometry from broadband images in a similar wavelength region. We fit the continuum measurements to a one-dimensional light

profile, as described in Bershady et al. (2005). They report this photometric method delivers centering precision of 0.25 arcsec with a similar IFU (SparsePak; Bershady et al. 2004). This precision is comparable to the velocity-field fitting (kinematic) method, and allows us to place the IFS observations on an astrometric scale without making any assumptions about how light traces mass. In Figure 5, we show the radial profiles of the DensePak continuum flux adopting both the kinematic and photometric centers. By construction, the radial profiles appear tighter when adopting the photometric centers, but the difference is typically not that large, particularly compared to the change between adopting the telescope offsets to either the kinematic or photometric centers. This similarity between radial profiles adopting either kinematic or photometric centers is an indication that the two measurements of the pointing offsets are similar.

We illustrate the difference between kinematic and photometric centers more quantitatively in Figure 6. This figure shows

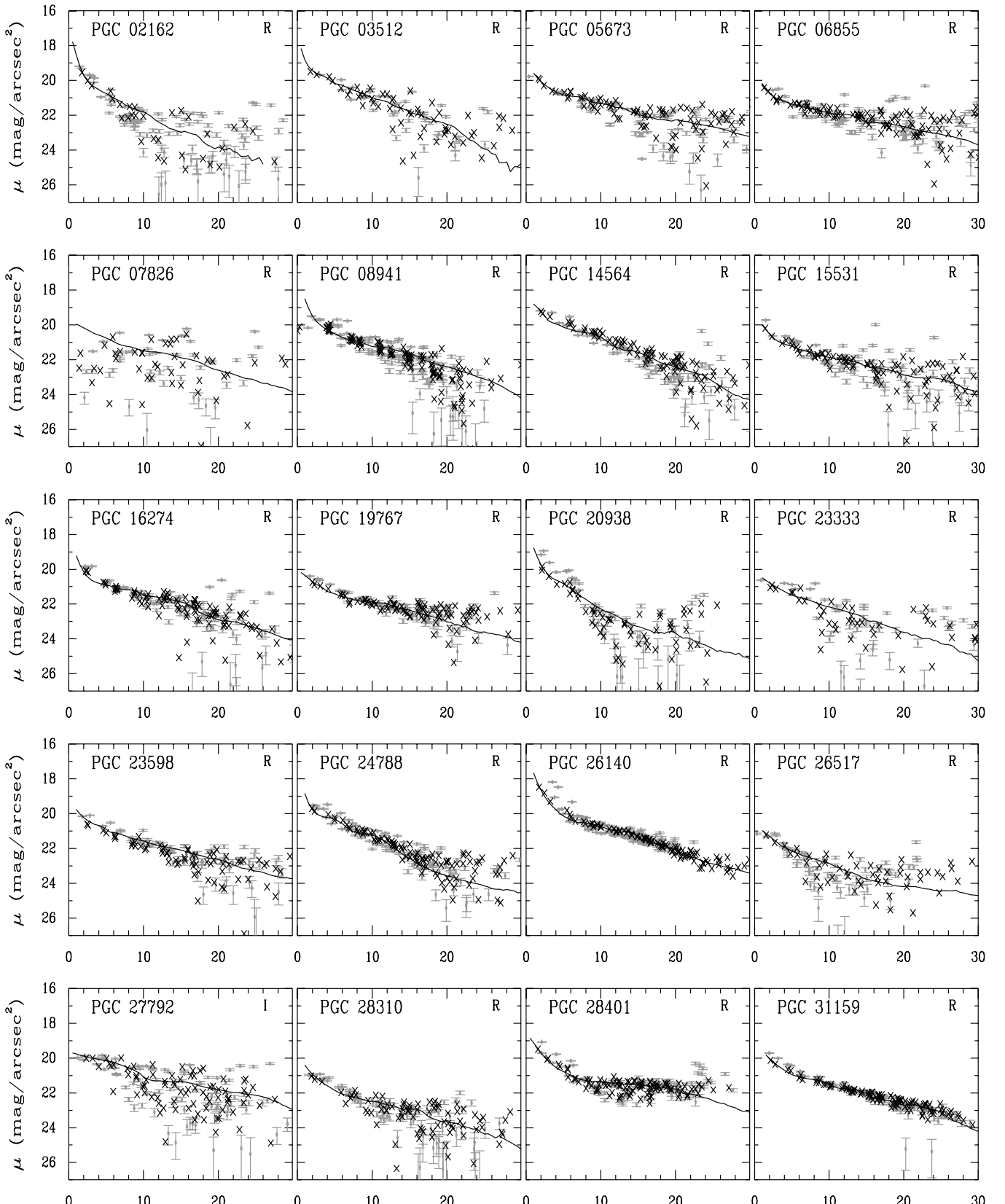


Figure 5. Surface brightness profiles for the sample galaxies derived from photometrically calibrated imaging (solid line) and from the DensePak continuum (with zero points chosen to match the imaging). Imaging was in the R band except for PGC 27792 and PGC 32091 which use I -band imaging (as noted in the top right of each panel). Continuum surface brightnesses were measured between $6600 \text{ \AA} < \lambda\lambda < 6800 \text{ \AA}$. Radial surface brightness profiles combine measurements from two or more DensePak pointings. For the lighter gray points, the centers and telescope offsets are determined from velocity-field modeling. For the black points overlayed on top, the center and offsets were determined by the photometric fitting technique described in Section 3.2. While the black points have small scatter by construction, the surface brightness profile delivered from the kinematic offsets and center are not much different, indicating that these kinematic centers and offsets should be sufficiently accurate.

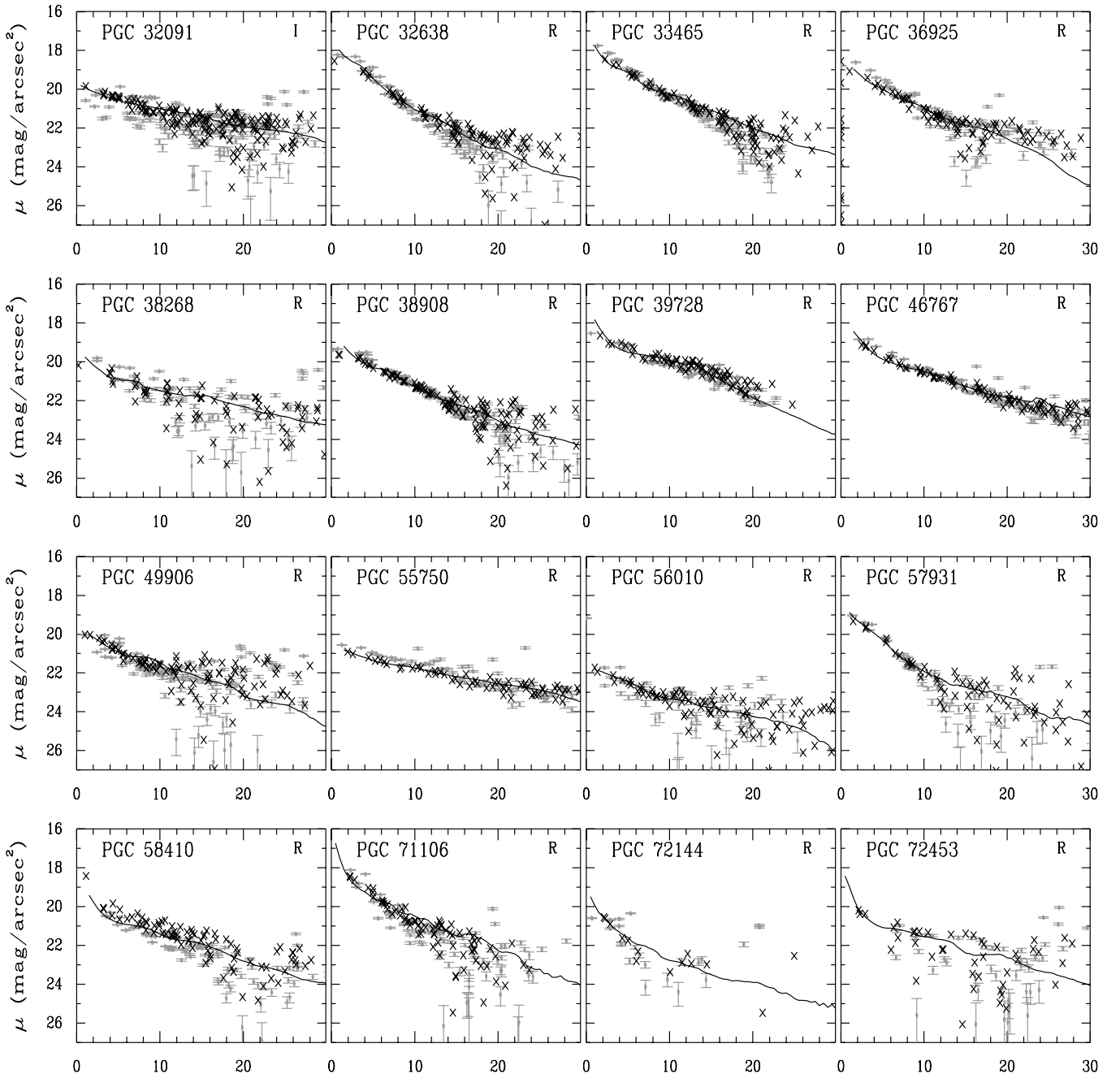


Figure 5. (Continued)

both the mean difference between kinematic and photometric centers for all pointings for a given galaxy, as well as the variations with respect to this mean from pointing to pointing for each galaxy. The latter is equivalent to looking at the differences between kinematic and photometric offsets, pointing-by-pointing. Both quantities, taken over the full sample, are expected to have average values of zero, which they do. Some individual galaxies in the left panel of Figure 6 appear to have significant mean differences between kinematic and photometric centers, similar to other studies (Andersen et al. 2008; Neumayer et al. 2011). In some cases, this may be due to true variations between the centers of light and the barycenters. In other cases, the variations may be due to systematics in one fitting method or the other. This is a point we return to in Section 4.2. Looking instead at the variations between kinematic and photometric offsets removes these systematic effects. The rms distribution of

offset differences (kinematic minus photometric; right panel of Figure 6) based on this comparison is characterized by a mode of 0.35 arcsec, but a mean of 0.7 arcsec due to a tail that extends to 2 arcsec and contains 10% of the sample. This tail is likely due to the failure of one of the centering methods, a related point that we return to in Section 4.2. After re-fitting the velocity fields with the photometric centers and offsets fixed, we did not find significant changes in the other kinematic parameters, even for those galaxies in this sample with the largest differences between kinematic and photometric positions.

3.3. Velocity-field Parameter Error Estimation

In general, once galaxies were fit with our simple velocity field and the reduced- χ^2_{δ} was unity (Equation (6)), we assumed the error distribution was Gaussian and used the standard

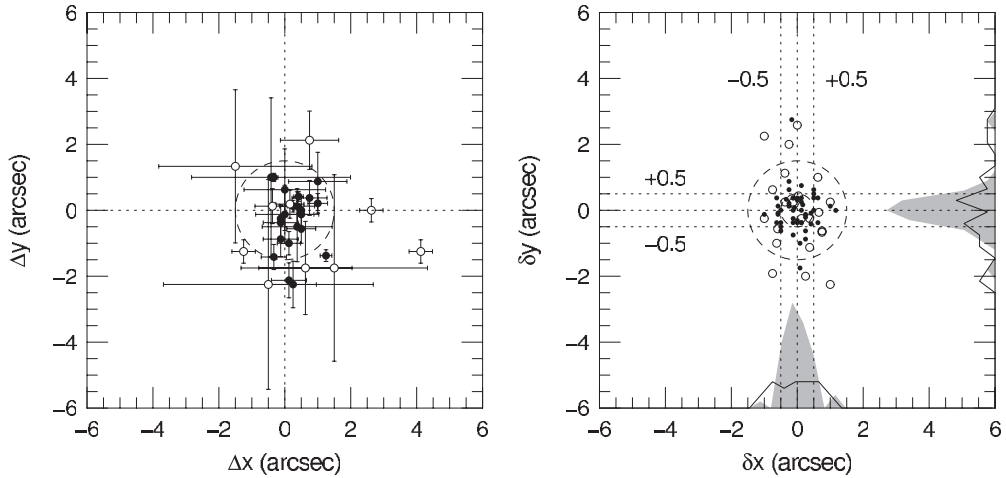


Figure 6. Differences between photometric and kinematic centers. Left panel: mean difference of all IFU pointings for a given object for each of 39 galaxies in this study. Error bars represent the dispersion in the mean. Right panel: offset of each pointing from the mean difference for a given object, for all pointings and all objects. Solid symbols represent galaxies with symmetric velocity fields; open symbols represent galaxies with high degrees of asymmetry (10% or larger in velocity). The dashed circle in both panels is the DensePak footprint. Marginal histograms are gray filled for kinematically regular galaxies, and open (black line) for kinematically asymmetric systems. Dotted lines on the axis and offset by ± 0.5 arcsec are for reference.

differences in χ^2 to map out confidence intervals in parameter space. Marginalizing over errors in relative position, recession velocity, and position angle, we map χ^2 of inclination versus rotation speed for the entire sample. The covariance between these two parameters is not extreme, and is the strongest observed from the sample. Therefore, except for inclination and rotation speed, we were able to calculate a changing χ^2 while varying a single parameter to determine errors. Model parameter errors quoted in Table 3 are from the 68% confidence intervals.

4. VELOCITY-FIELD STRUCTURE

Observations of spiral galaxy velocity fields reveal a large variety of non-circular motions. As described in the Introduction, these motions include large-scale asymmetries, motions associated with individual spiral arms, solid body rotation, and kinematic warping. After examining the residuals to our model velocity-field fits (Figure 7) for the kinematic signatures of these non-circular motions, we found evidence for kinematic asymmetry and streaming motions associated with spiral arms (see Figure 8 for an example). However, we do not find evidence for solid body rotation or kinematic warping in our sample. Solid body rotation is a signature of barred galaxies, so our selection of unbarred galaxies mitigates the impact this effect would potentially have on our velocity fields. Kinematic warping, manifested by a twisting of the kinematic position angle with radius, is exhibited in a large fraction of disks at large radii. Few galaxies in other surveys show signs of warping within three scale lengths (Briggs 1990; van der Kruit 2007; Saha et al. 2009; Guijarro et al. 2010). Since this is where we measure H α emission for our sample, it is not surprising to find a lack of evidence for warping.

4.1. Projected Rotation Curves

As a complement to the full velocity fields presented in Figure 1, we also produced H α major-axis position–velocity diagrams for our sample to better study characteristics of disk structure. We included fibers with positions up to 60° off the major axis in the galaxy plane. To do this, we corrected velocities for fibers off the major axis by the $\cos\theta$ off-axis projection (Equation (1)), and placed them in radius according

to Equation (2). While this correction takes into account the inclination and position angle from the kinematic fits to the velocity fields in Figure 9, we make no correction for the projection due to inclination alone. It is difficult to distinguish between data from different regimes in θ . The exercise shows the accuracy of the kinematic model: by using the kinematic inclinations, centers, and position angles, DensePak fiber data taken from positions specified by R and θ in the galaxy plane can be corrected for azimuthal projection to yield rotation curves with small residuals from either the tanh or pseudo-isothermal sphere rotation-curve models (Equations (4) and (5)). For most galaxies, it is not possible to distinguish the quality of fit between the two models. However, one difference in the fits is that the tanh rotation-curve model quickly rises to its asymptotic flat velocity, v_{rot} , for these data, while the pseudo-isothermal sphere model is still slowly rising for almost all galaxies.⁴ As we shall see in Section 5.3, this discrepancy between v_{rot} and v_{pISO} will call into question the physical validity of the pseudo-isothermal sphere fits to these data.

4.2. Rotation-curve Asymmetry

We explore general kinematic asymmetries for our sample in the specific context of the projected rotation curves. To measure rotation-curve asymmetries, we adopt the formulation of Dale et al. (2001):

$$A_{\text{RC}} = \sum \frac{||V(R)| - |V(-R)||}{[\sigma^2(R) + \sigma^2(-R)]^{1/2}} \sqrt{\frac{1}{2} \sum \frac{|V(R)| + |V(-R)|}{[\sigma^2(R) + \sigma^2(-R)]^{1/2}}}, \quad (7)$$

where $V(R)$ was the velocity at each point in the rotation curve and $\sigma(R)$ was the error on that velocity. To measure A_{RC} from our data, we first subtract V_{sys} from each velocity measurement, and project each velocity measurement with $|\theta| < 60^\circ$ onto the major axis. We then calculate the weighted mean velocity in 5 arcsec width bins before finally summing A_{RC} over all

⁴ The only galaxy for which v_{rot} is more than 10% larger than the maximum observed velocity is PGC 24788. The mean observed velocity on the major axis 20 arcsec from the field center is 69 km s^{-1} , while v_{rot} is 85 km s^{-1} . The rotation curve of PGC 24788 is still rising, but given the H α line widths measured in Paper II, it seems likely that v_{rot} is too large. The value of $v_{\text{pISO}} = 97 \text{ km s}^{-1}$ is greater still.

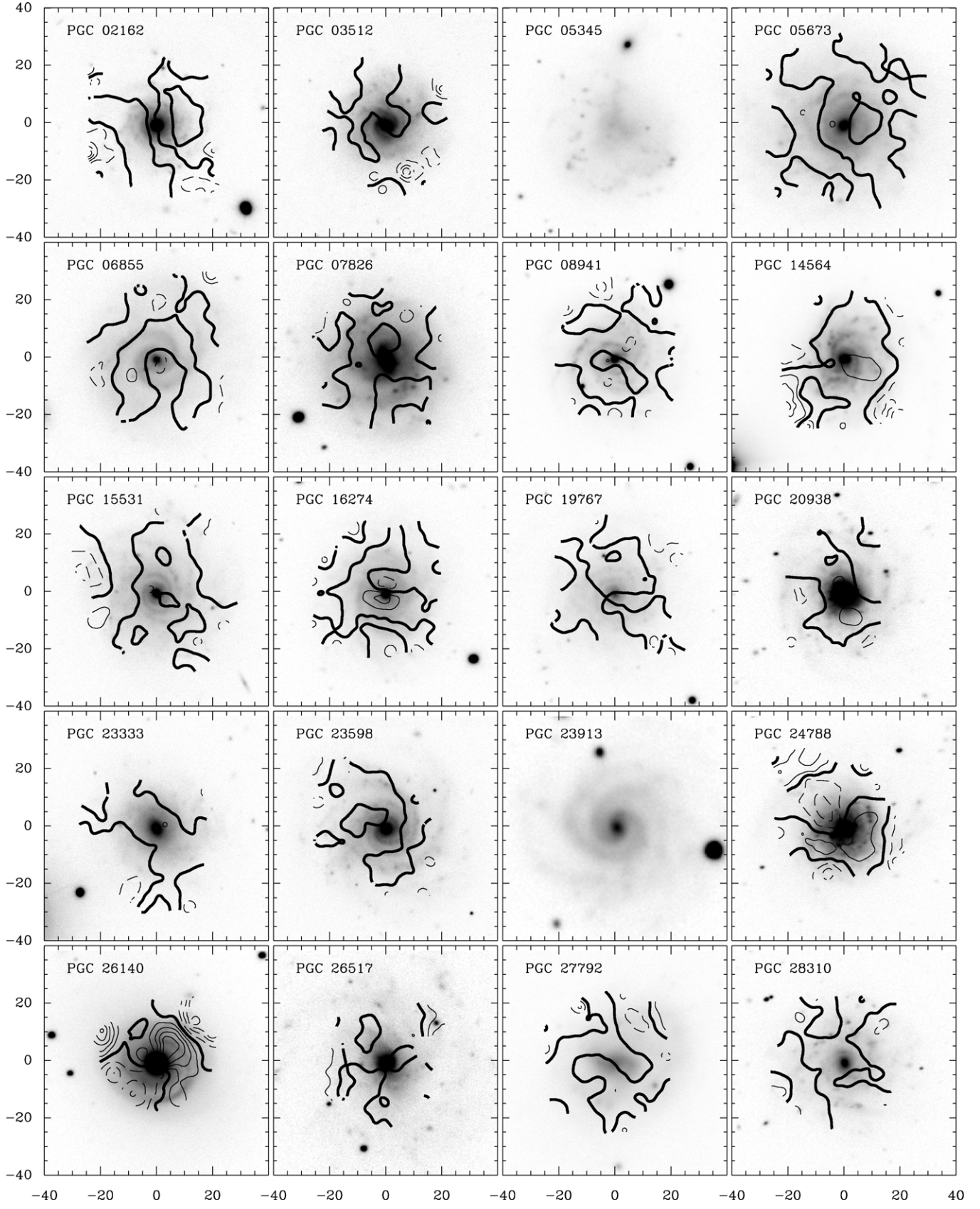


Figure 7. Residual velocity contours after fitting a single, inclined-disk model to the velocity fields shown in Figure 1. The heavy solid lines mark the zero difference between model and observation. Lighter solid lines represent positive deviations in the difference of observation and model velocity fields, and dashed lines represent negative differences. The spacing of the iso-velocity difference contours is just 3 km s^{-1} . There are no contours on the PGC 5673, PGC 23913, and PGC 70962 images because these galaxies were not successfully fit by the model.

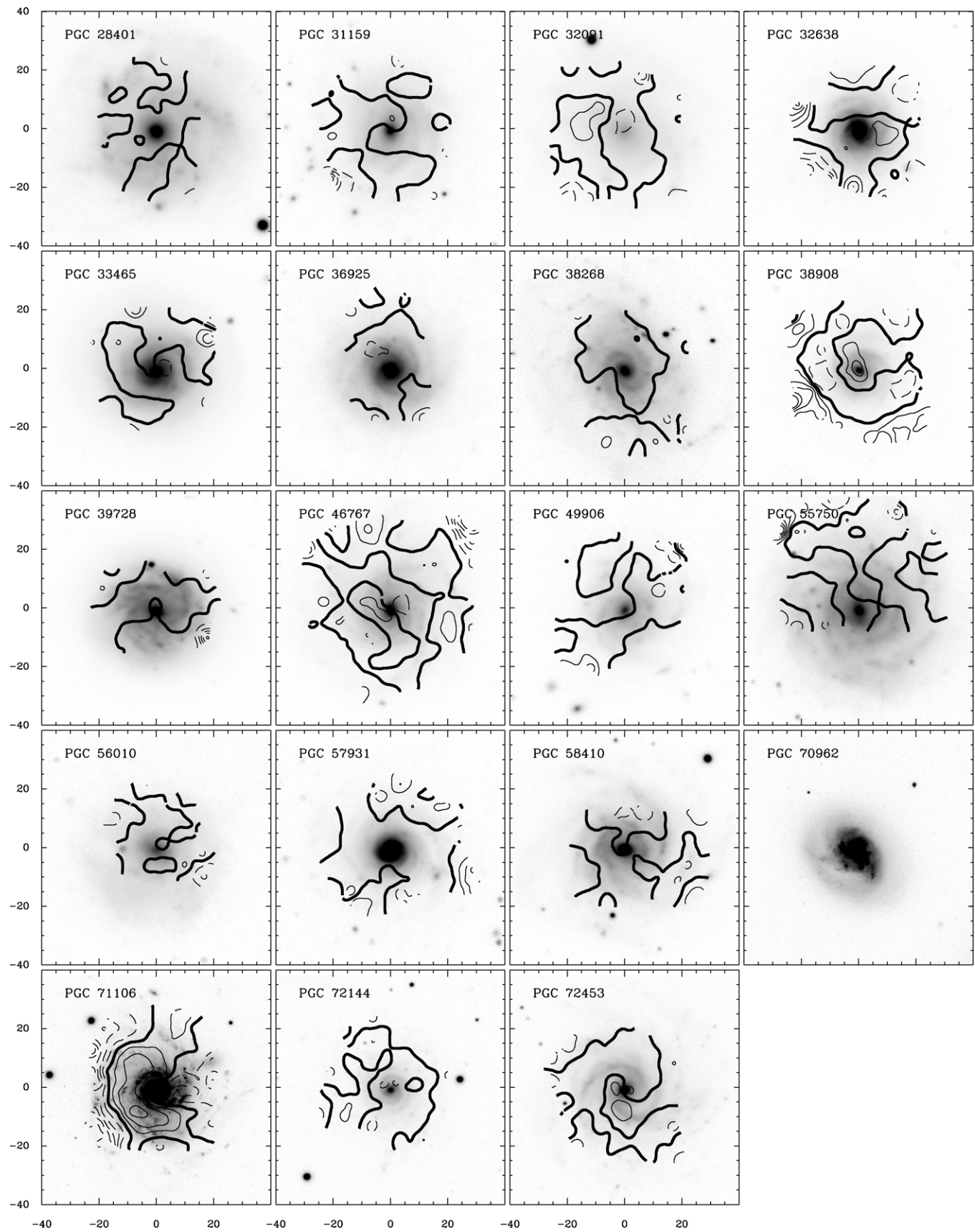


Figure 7. (Continued)

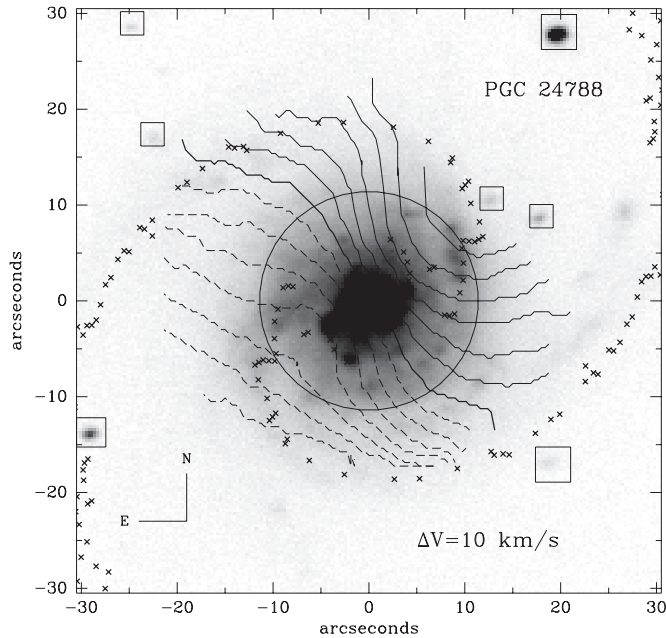


Figure 8. Velocity field of PGC 24788, which shows twisting associated with spiral arms. Spiral arms are emphasized by x's marking the position angle of the ellipse that best fits the surface photometry at each radius. The circle has a radius of 12 arcsec.

radii for which data exist on both sides (Table 3). Note that this index is a ratio of velocity differences and hence is independent of the amplitude of the rotation curve and its projection due to inclination. Eight galaxies in our sample exhibited significant asymmetries: PGC 6855, PGC 20938, PGC 24788, PGC 28401 (mainly because the projected rotation speed is less than 10 km s^{-1}), PGC 32091, PGC 49906, PGC 56010 (which has an incomplete set of DensePak pointings), and PGC 71106. If we exclude PGC 28401 and PGC 56010 for the reasons just mentioned, we found that the mean $A_{\text{RC}} = 0.06 \pm 0.04$ (much less than the mean value of $A_{\text{RC}} = 0.14$ reported by Dale et al. 2001 for a sample of cluster spiral galaxies). The relative non-asymmetric nature of our sample is in keeping with its selection (as described in Paper I). The observed rotation-curve asymmetries are uncorrelated with the skewness (lopsidedness) of the global H α profiles reported in Andersen & Bershady (2009).

One evident correlation exists between the amplitude of the rotation-curve asymmetry and the degree to which kinematic and photometric centers (Section 3.2) agree. This is hardly surprising. For example, PGC 24788, a galaxy with a H α velocity field showing strong twisting associated with spiral arms (Figure 8), has the most discrepant centers. In this case the kinematic method is likely more suspect because it is based on a fit to an axisymmetric model. In general, galaxies with large asymmetries in their rotation curves ($>10\%$ in velocity) show systematically larger offset differences, as illustrated in Figure 6. More symmetric galaxies have photometric and kinematic centers that typically agree to within 0.5 arcsec (roughly 120th of a radial scale length). Whether the increased discrepancy between photometric and kinematic centers with rotation-curve asymmetry is due to systematics in the measurements (which adopt a symmetric model), or to actual barycenter offsets from the center of light requires further investigation.

4.3. Velocity-field Asymmetry

Theoretical calculations of gas shocks in spiral arms suggest that a perturbation in the velocity field on the order of 10 km s^{-1}

should be association with massive spiral arms (e.g., Roberts 1969; Dobbs et al. 2011). This kinematic signature of spiral arms can be obfuscated by $10\text{--}15 \text{ km s}^{-1}$ velocity fluctuations in the gas caused by turbulence and expanding supernovae shells (e.g., Beauvais & Bothun 1999; Bagetakis et al. 2011). Only a few unbarred galaxies show a strong kinematic signature associated with spiral arms (e.g., Visscher 1980; Kranz et al. 2001; Shetty et al. 2007). Indeed, our pilot study of seven galaxies showed little evidence for radial or azimuthal variations in the residuals of the velocity-field model (Andersen et al. 2001). There was evidence that PGC 46767 showed a small sinusoidal variation in the fit residuals, but the phase of the sinusoid was unmatched to the spiral arms. This non-detection of spiral arms was unsurprising; we chose galaxies with very weak spiral arms for the pilot study in order to facilitate measurements of photometric axis ratios and position angles. For the selection of galaxies in this larger sample, we relaxed the requirement on spiral arm strength, which was qualitative anyway. As a result, we found six galaxies that showed sinusoidal variations in azimuthal residuals from velocity-field models. These variations are likely evidence for streaming motions along their spiral arms. Galaxies which exhibited this signature include: PGC 14564, PGC 24788, PGC 26140, PGC 38908, PGC 46767, and PGC 71106.

To isolate this affect, we show the azimuthal variation in velocity for radii greater than $1.5 h_{\text{rot}}$ (Figure 10). The smoothed residuals exhibit systemic variations in residual with the azimuthal angle, but these residuals are not consistent in phase with inclination errors. Quantitatively, we measure the weighted mean of the absolute difference between model and measured velocities, at radii greater than $1.5 h_{\text{rot}}$, normalized by v_{rot} , which we call A_{ϕ} (Table 3).

The unnormalized quantity, $A_{\phi} \times v_{\text{rot}}$, is greatest for those galaxies listed above which have velocity fields that qualitatively shows the signatures of flows due to spiral structure. These galaxies do not appear to be significantly asymmetric, however, when considering the normalized quantity A_{ϕ} . The distribution of A_{ϕ} for galaxies in our sample ranges from 0.02 to 0.3 (Figure 11), with a mean of 0.06 and standard deviation of 0.04. In other words, these galaxies have random ionized-gas motions of roughly 6% of their circular speed. Galaxies in our sample with the largest azimuthal asymmetries ($A_{\phi} > 0.1$) tend to have very small projected rotation velocities, and include PGC 7826, PGC 28401, and PGC 56010. The remaining galaxies with above-average azimuthal asymmetries ($0.06 < A_{\phi} < 0.10$) include PGC 2162, PGC 24788, PGC 26517, PGC 27792, PGC 32091, and PGC 49906.

We find that this A_{ϕ} asymmetry measure is uncorrelated with the skew measured from the integrated H α profiles (Andersen & Bershady 2009), although PGC 7826 has large skew and large A_{ϕ} values. This suggests that the asymmetries in the global H α profiles are dominated by asymmetries in the distribution of ionized gas and not by kinematic asymmetries. This conclusion echoes our results from Andersen & Bershady (2009), in which we show using H α imaging for a subsample of these galaxies, that the skew (asymmetry) in the H α global profiles can be almost wholly attributed to the asymmetric distribution of ionized gas.

4.4. Correlations between Asymmetry Measures

Given the definition of A_{ϕ} and A_{RC} , derived from the same data, it is unsurprising that the two quantities are well correlated, as illustrated in Figure 11. Typical values (both normalized to

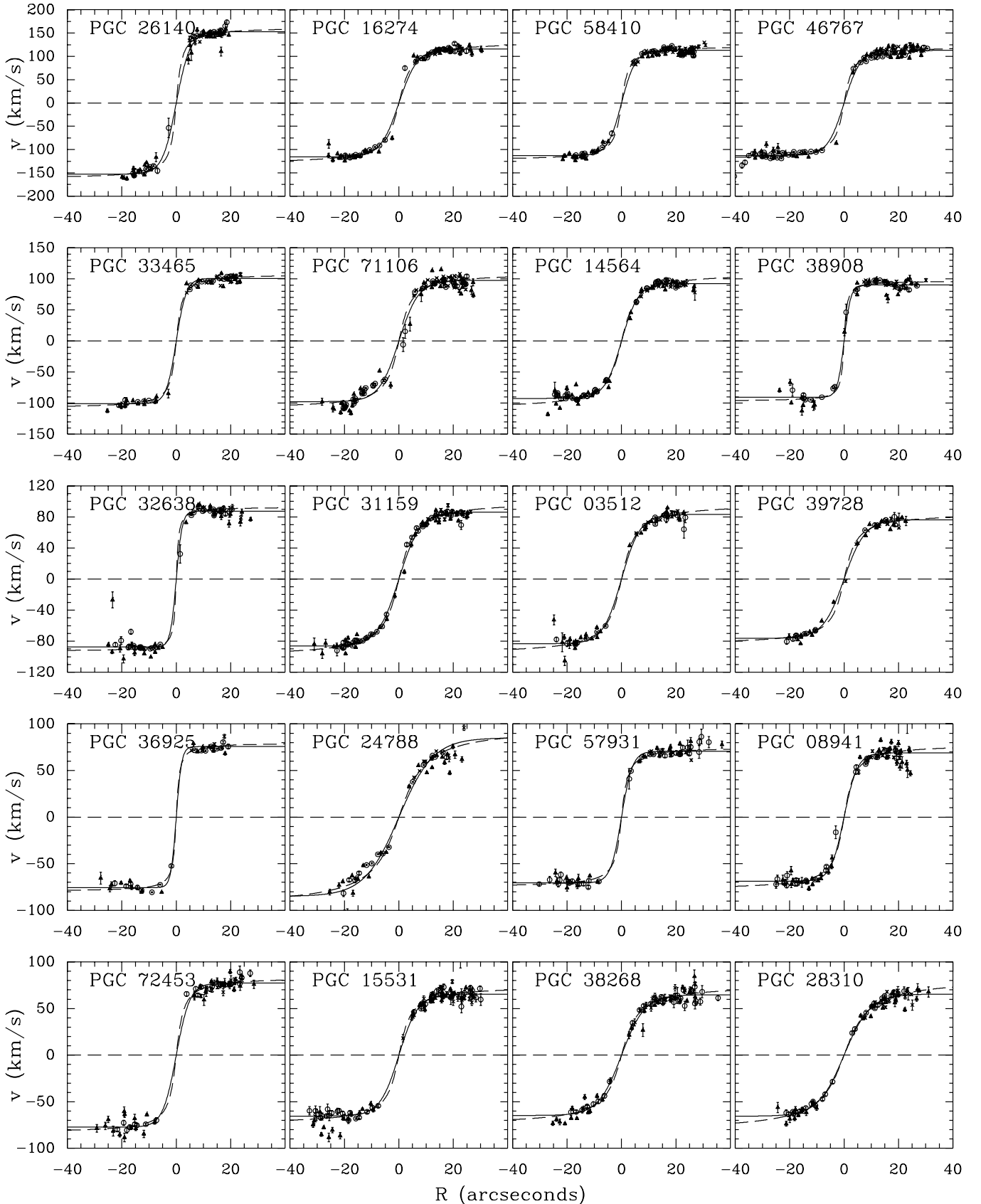


Figure 9. Position–velocity diagrams deprojected to the major axis (but not for inclination) for the sample sorted by decreasing projected rotation speed. After fitting velocity-field models to the data, each DensePak velocity centroid can be projected to the major axis radius, R , where R is measured in the galaxy plane. Positions $|\theta| < 20^\circ$, where θ is the angle from the major axis in the galaxy plane, are marked with dark, open circles. Slightly lighter x's mark data $20^\circ < |\theta| < 40^\circ$. Light filled triangles mark data $40^\circ < |\theta| < 60^\circ$. The solid lines mark the model hyperbolic tangent rotation curve (Equation (4)). The dashed lines correspond to the pseudo-isothermal model (Equation (5)).

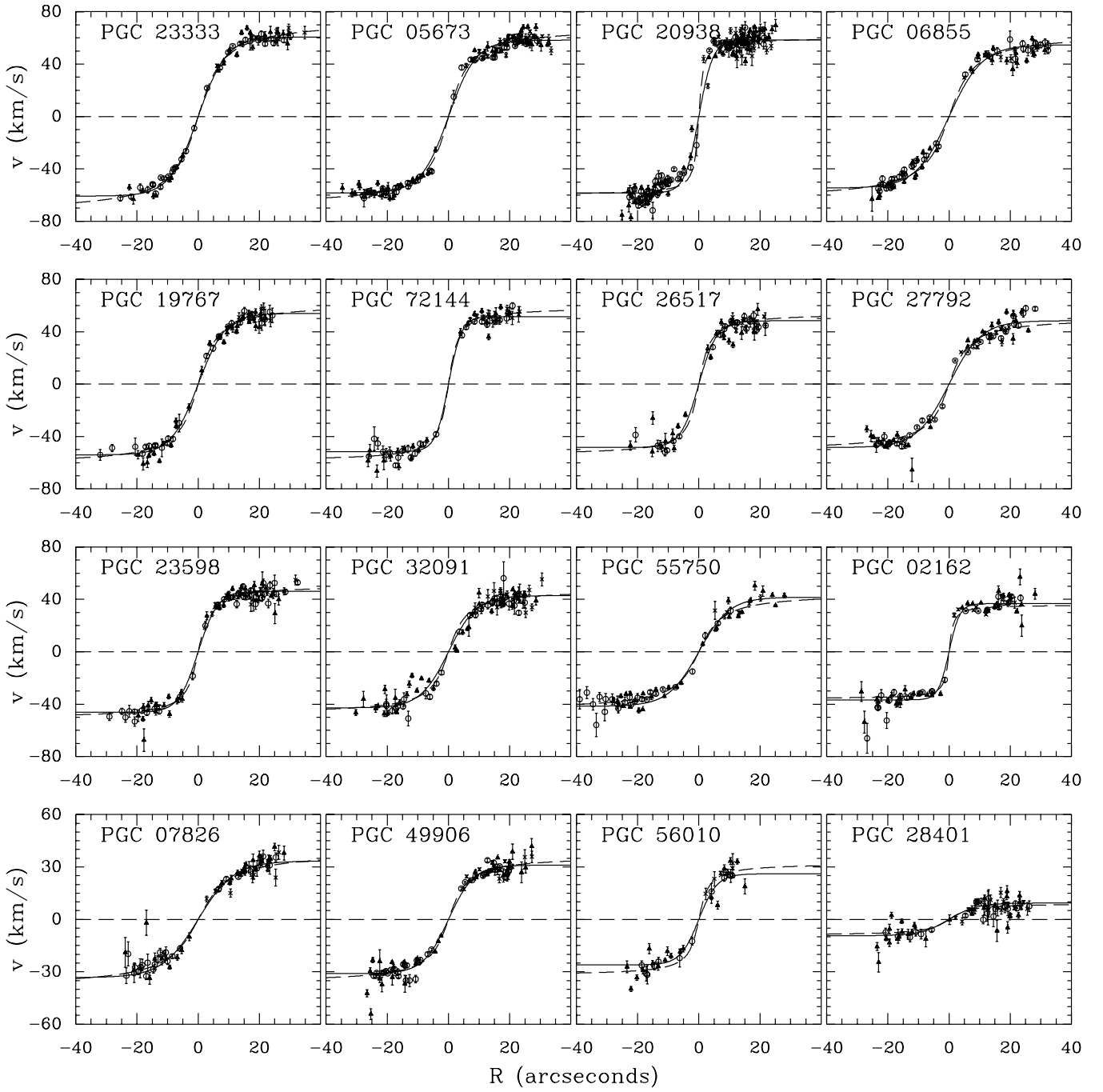


Figure 9. (Continued)

the terminal amplitude of the projected rotation curve) differ by about 41% (rms). This implies that a substantial fraction of the azimuthal asymmetry, A_ϕ , is due both to a low-order (e.g., $m = 1$ or lopsided mode) perturbation as measured by A_{RC} , as well as higher-order modes. Future analysis will further quantify the power in these different modes.

A tighter correlation exists between A_ϕ and $\sigma_{\text{mod}}/v_{\text{rot}}$, with an rms variance of only about 20%. This indicates that our interpretation and reasoning for adding the σ_{mod} to our definition of χ^2 is physically plausible, i.e., σ_{mod} is a measure of the deviation from pure circular motion of the ionized gas. This correlation and interpretation are important for what follows in our evaluation of the kinematic estimates of inclination.

5. EVALUATION OF INCLINATION ESTIMATES

5.1. Accuracy of Kinematically Estimated Inclinations and Inclination Errors

Because differences in model velocities at low inclination are relatively small (Figure 4), we simulated whether we could measure accurate inclinations for $i < 30^\circ$. We created Monte Carlo simulations of typical DensePak data using Equations (1)–(4) and Gaussian uncertainties on the velocities. After fitting these simulated data, as described above, we were able to determine the standard deviation of model parameters. The resultant estimates of expected inclination errors as a function of inclination were surprisingly small: at $i = 15^\circ$, we expected $\Delta i \approx 5^\circ$.

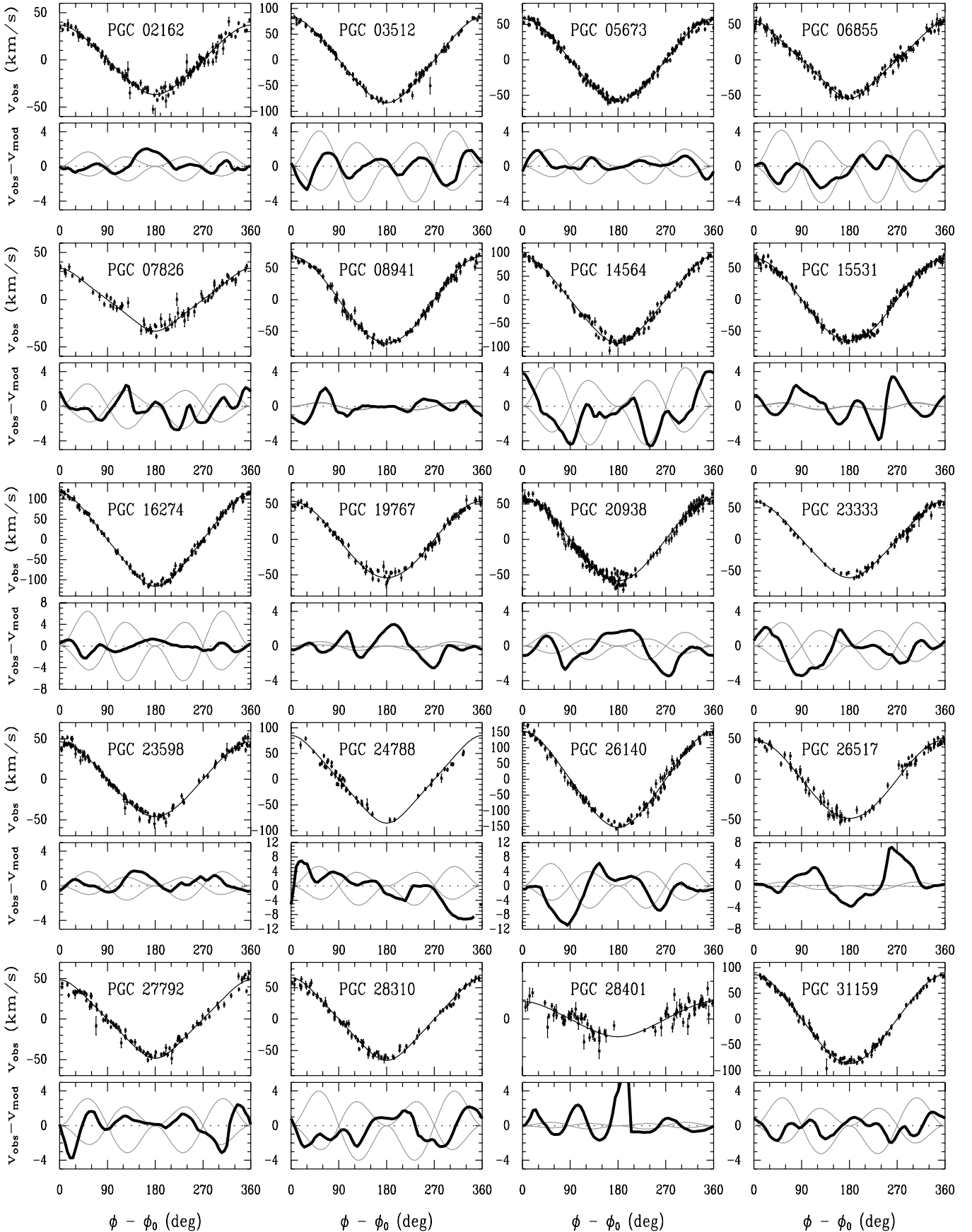


Figure 10. Azimuthal variation in observed velocities (top panel) for each galaxy with a velocity-field fit. Model velocities are plotted as a solid line for those points beyond $1.5 h_r$ (on the flat part of the rotation curve). Smoothed residuals are shown (lower panel; heavy solid line), with the differences one would expect for a velocity-field model with inclinations differing by $\pm 10^\circ$ (light gray lines). Smoothing was done using a Hanning (sawtooth) filter with width of 60° . Residuals are uncorrelated in phase with inclination errors, but in some cases (e.g., PGC 14564 or PGC 24788) these residuals may be consistent with streaming motions along spiral arms.

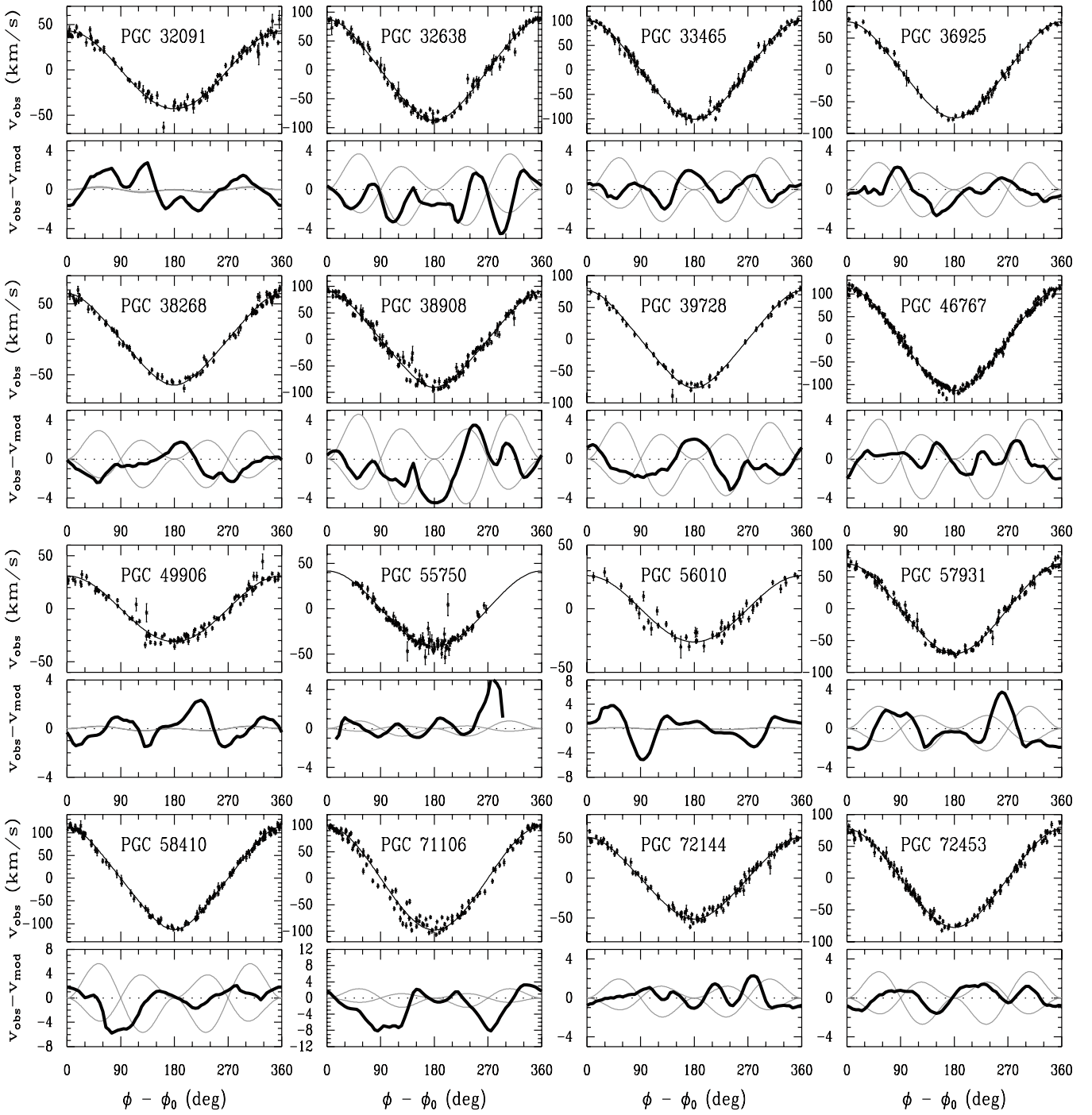


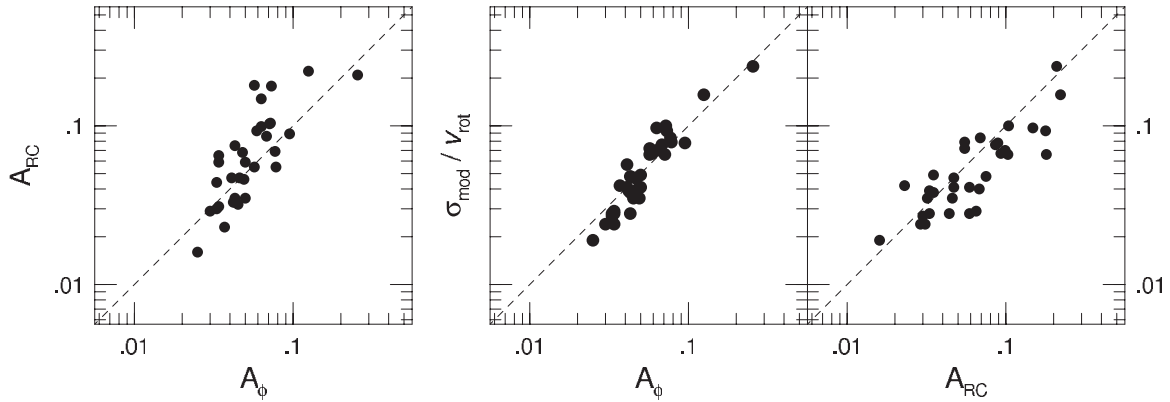
Figure 10. (Continued)

for typical DensePak data. Errors estimated for most individual galaxies (Table 3) matched our Monte Carlo simulations, but several galaxies had unexpectedly high inclination errors, given their nominal inclinations, when compared to our expectations from the Monte Carlo simulations. These galaxies included PGC 6855, which has an asymmetric rotation curve; PGC 24788, which has a strong spiral distortion; PGC 28401, which has $v_{\text{rot}} = 8 \text{ km s}^{-1}$ and has an inclination errors consistent with $i = 0$; and PGC 56010, which has only 70 velocity measurements, un-centered on the galaxy. In short, in each case there are good reasons for the errors to be larger than what otherwise would be typical. However, this exercise motivated a

more thorough examination of the reliability of our kinematic inclinations and their errors.

5.2. Inclinations from the Tully–Fisher Relation

We have independent information that can be used to check and refine our kinematic inclination measurements. The Tully–Fisher relation between a galaxy’s rotation speed and its absolute magnitude provides a completely separate constraint on inclination and rotation speed. To estimate inverse TF inclinations, we used the published *R* and *I* bands TF relations from Verheijen’s (2001) “RCFD” sample of 21 galaxies (excluding

Figure 11. Comparison of kinematic asymmetry estimates A_ϕ , A_{RC} , and σ_{mod} .

NGC 3992) in Ursa Major

$$M_R = 2.81 - 9.6 \log 2V_{\text{flat}} \quad (8)$$

and

$$M_I = 4.27 - 10.4 \log 2V_{\text{flat}}. \quad (9)$$

We therefore can estimate $v_{\text{rot}}/\sin i \approx V_{\text{flat}}$ based on the absolute R - and I -band magnitudes from the imaging data (Table 1; Section 2.2). We derived absolute magnitudes based on distance moduli (DM, 1) assuming $H_0 = 73 \text{ km s}^{-1} \text{ Mpc}^{-1}$, the recession velocities (Table 3), and a correction for Virgo infall from HyperLeda (Paturel et al. 2003).⁵ (Note that a value of $H_0 = 77 \text{ km s}^{-1}$ is used to set distance to the Ursa Major cluster; Tully & Pierce 2000; see below.) We applied no k -corrections, since these are negligible (<0.01 mag) for disk galaxies at these redshifts (e.g., Bershady 1995). To match Verheijen's (2001) photometric scheme, further corrections to the magnitudes were made for Galactic extinction (A_R and A_I in Table 2; Schlegel et al. 1998) and internal extinction, with the latter following the explicit prescription in Verheijen (2001). Assuming our sample has inclinations of 23 ± 8 deg (based on our kinematic estimates), the internal-extinction corrections amount to 0.22 and 0.16 mag, on average, in the R and I bands, with a variance of under 0.02 mag for the full inclination range. While the prescription for internal-extinction corrections is designed for application to more inclined systems, recent work by Schechtman-Rook et al. (2012) has shown that while this estimated internal-extinction correction is on average too large at any given inclination, the relative trend in internal extinction versus inclination is a good match to realistic radiative-transfer models of intermediate-to-late-type disk galaxies. This relative consistency with inclination is therefore adequate for our purpose. The inferred inverse TF inclinations (i_{TF}) are given in Table 4.

To calculate the uncertainties in i_{TF} , we include all known sources of uncertainty into the error budget for our absolute magnitudes. The errors quoted in Table 4 include random errors on the photometry and uncertainties in the flow correction (we estimate $\pm 150 \text{ km s}^{-1}$), Galactic extinction (we estimate 10% of the correction, or $\pm 0.1A$), k -corrections (or lack thereof, ± 0.01 mag), and internal extinction (± 0.02 mag). To this we add in quadrature the intrinsic scatter in the TF relation, assuming it is random; we adopt ± 0.2 mag scatter, which is the mean of values estimated by Verheijen (2001) for either band estimated with and without Ursa Major depth corrections.

All of the above uncertainties arguably produce random errors in i_{TF} , because the sign and amplitude of each will vary from

galaxy to galaxy. For the purpose of comparing to the kinematic and photometric inclinations, we also include these sources of systematic error in i_{TF} : the uncertainty in the distance to Ursa Major due to its depth (0.04 mag based on 0.17 mag depth and 21 galaxies); and the uncertainty in H_0 (7% in distance, or 0.15 mag). We also find a systematic difference of 0.4 ± 0.2 deg between i_{TF} determined from the R versus the I bands. We add this difference as an additional uncertainty, in quadrature. The uncertainties on i_{TF} listed in Table 4 include all of these sources of error.

We produced a Monte Carlo simulation that demonstrates the nature of inclination errors for various methods (Figure 12; Monte Carlo simulations of kinematic inclinations are discussed in Section 5.3 and photometric inclinations are discussed in Section 5.4). We generated a sample of galaxies with a uniform distribution of true inclinations between 0° and 40° . Galaxies had absolute R -band magnitudes chosen uniformly between -19 and -23 (matching the range in our sample). We included 0.25 mag of measurement error and TF scatter. These simulations seem to indicate that the inverse TF inclinations appear to be both quite accurate and precise. Scatter between the inverse TF and the true inclinations increase with inclination, as expected. Galaxies which are outliers from the TF relation, or are very late-type, such as PGC 5345, and may not yet be rotationally supported are not included in the Monte Carlo simulations and would show significant deviations between the true inclination and the inverse TF inclination. For most galaxies in our sample, however, we suspect that the inverse TF inclinations should be a very good indication of the true inclination.

5.3. Comparing Kinematic to Inverse TF Inclinations

An initial comparison between kinematic and inverse TF inclinations (Figure 13) shows a large scatter, but this can be quickly reduced by considering two basic criteria.

First, kinematic inclinations fail when there is insufficient curvature in the iso-velocity contours. This occurs because either the rotation-curve shape is too close to solid body (for which there is no curvature); the galaxy is too close to face-on (the curvature is small compared to the random errors); the non-circular motions are too large (the global curvature due to inclination is small compared to random motions); or any combination of the above. The failure is manifest when the kinematic inclination estimate is consistent with zero within, say, the 68% confidence level (CL), yet the galaxy clearly displays projected rotation. In this regime, there is additional information (non-zero projected rotation) that clearly tells us the kinematic inclinations and their errors are failing. We indicate

⁵ <http://leda.univ-lyon1.fr/>

Table 4
Comparison of Inclination Measurements

PGC	i_{phot} (deg)	$i_{\text{TF}}(R)$ (deg)	$i_{\text{TF}}(I)$ (deg)	i_{kin} (deg)	A_{ϕ}/v_{rot} ($\times 10^{-4}$ km $^{-1}$ s)
2162	...	15.7 ± 1.0	15.8 ± 0.9	29.1 $^{+4.7}_{-6.4}$	21.0
3512	22.0 ± 4.6	30.8 ± 1.9	31.1 ± 1.8	31.1 $^{+2.3}_{-2.4}$	4.1
5673	25.2 ± 1.9	22.6 ± 1.4	23.0 ± 1.3	22.0 $^{+3.1}_{-3.9}$	7.0
6855	27.6 ± 3.6	22.5 ± 1.4	22.7 ± 1.3	43.6 $^{+2.3}_{-3.0}$	10.4
7826	...	18.8 ± 1.3	18.4 ± 1.2	44.1 $^{+4.5}_{-4.7}$	28.5
8941	15.2 ± 3.7	18.1 ± 1.1	19.0 ± 1.1	0.3 $^{+9.9}_{-0.3}$	6.1
14564	...	31.8 ± 2.2	34.0 ± 2.2	30.6 $^{+2.9}_{-3.2}$	4.6
15531	32.9 ± 2.8	25.8 ± 1.6	26.6 ± 1.5	0.6 $^{+8.9}_{-0.6}$	7.6
16274	26.7 ± 2.0	35.5 ± 2.2	35.4 ± 2.1	34.4 $^{+1.7}_{-1.7}$	2.2
19767	30.2 ± 3.9	23.1 ± 1.4	22.7 ± 1.3	3.1 $^{+9.2}_{-3.1}$	9.1
20938	...	28.1 ± 1.8	...	16.9 $^{+5.0}_{-8.7}$	10.8
23333	21.9 ± 2.8	24.9 ± 1.5	...	28.6 $^{+3.2}_{-4.3}$	7.4
23598	24.8 ± 3.8	14.6 ± 0.9	14.9 ± 0.9	22.8 $^{+4.5}_{-6.4}$	10.8
24788	...	27.4 ± 1.7	28.8 ± 1.7	38.2 $^{+4.9}_{-4.9}$	8.4
26140	37.1 ± 1.3	38.8 ± 2.5	42.3 ± 2.7	26.1 $^{+3.2}_{-2.8}$	2.8
26517	...	26.8 ± 1.7	27.7 ± 1.6	7.0 $^{+15.5}_{-7.0}$	16.1
27792	38.0 ± 2.1	38.7 $^{+3.8}_{-5.1}$	14.0
28310	24.9 ± 4.9	...	29.6 ± 1.7	37.1 $^{+2.7}_{-2.7}$	6.6
28401	35.2 ± 2.2	3.5 ± 0.5	3.5 ± 0.5	27.0 $^{+9.0}_{-27.0}$	274.2
31159	33.9 ± 4.8	...	33.0 ± 1.9	24.0 $^{+2.8}_{-3.0}$	3.5
32091	25.8 ± 3.9	1.2 $^{+15.4}_{-1.2}$	17.0
32638	22.8 ± 3.7	27.5 ± 1.7	28.5 ± 1.6	26.9 $^{+3.6}_{-4.8}$	4.7
33465	18.9 ± 2.8	27.5 ± 1.7	...	20.7 $^{+3.3}_{-4.7}$	3.3
36925	21.4 ± 2.0	22.8 ± 1.5	23.2 ± 1.3	23.7 $^{+3.8}_{-4.9}$	4.5
38268	43.1 ± 2.8	32.7 ± 2.2	33.0 ± 2.0	28.9 $^{+3.8}_{-4.1}$	7.4
38908	24.8 ± 5.6	28.1 ± 1.7	31.1 ± 1.8	32.0 $^{+3.5}_{-3.9}$	6.3
39728	28.2 ± 1.3	35.2 ± 2.5	...	31.2 $^{+3.4}_{-4.1}$	4.4
46767	30.0 ± 1.5	27.3 ± 1.8	29.7 ± 1.7	23.3 $^{+2.5}_{-3.1}$	3.3
49906	19.9 ± 1.3	10.9 ± 0.8	11.2 ± 0.7	0.3 $^{+15.1}_{-0.3}$	23.2
55750	19.9 ± 3.0	16.6 ± 1.1	14.6 ± 0.9	10.6 $^{+9.4}_{-10.6}$	14.2
56010	...	16.0 ± 1.2	12.4 ± 0.9	1.0 $^{+28.0}_{-1.0}$	47.9
57931	27.6 ± 4.9	21.8 ± 1.3	24.5 ± 1.4	20.7 $^{+4.5}_{-6.5}$	6.5
58410	30.6 ± 3.2	33.7 ± 2.3	39.9 ± 2.4	31.6 $^{+2.0}_{-2.1}$	2.9
71106	29.6 ± 4.5	22.0 ± 1.3	23.2 ± 1.3	14.0 $^{+9.0}_{-14.0}$	6.4
72144	24.6 ± 6.3	18.0 ± 1.1	18.0 ± 1.0	24.4 $^{+5.2}_{-9.1}$	11.8
72453	...	21.7 ± 1.3	22.3 ± 1.2	22.4 $^{+3.8}_{-5.0}$	5.8

these objects in Figure 13 as red circles. The objects can be readily identified by inspection of Table 3 and Figure 9.

Second, the amplitude of non-circular motions clearly degrades the reliability of kinematic inclinations, even when the latter do not “fail.” As seen in Figure 13, there is a correlation between A_{ϕ} and v_{rot} which allows us to make cuts in the sample according the distribution in the ratio A_{ϕ}/v_{rot} . Galaxies with the largest values of A_{ϕ}/v_{rot} tend to be extreme outliers, even though they tend to also have larger errors in their estimated kinematic inclinations (Figure 14). We suspect that for galaxies with sufficiently large asymmetries, as parameterized by A_{ϕ}/v_{rot} , the kinematic modeling breaks down and the kinematic fits do not represent the true inclination or inclination error.

By removing half the sample with inclinations consistent with zero and the largest values of $A_{\phi}/v_{\text{rot}} > 8 \times 10^{-4}$ km $^{-1}$ s, we find the distribution of differences between kinematic and inverse Tully–Fisher inclinations ($\Delta i \equiv i_{\text{kin}} - i_{\text{TF}}$) approaches a

normal distribution given their estimated errors ($\sigma_{\Delta i}$). Including galaxies with larger values of A_{ϕ}/v_{rot} produces a significant non-Gaussian tail at large values of $\Delta i/\sigma_{\Delta i} > 3$. It makes sense that A_{ϕ}/v_{rot} is a superior performance indicator than either A_{ϕ} or v_{rot} alone since the kinematic fitting method requires both the amplitude of the projected rotation be large enough in an absolute sense (i.e., v_{rot}) relative to the random errors, and that the relative amplitude of the non-circular motions (relative to v_{rot} , i.e., A_{ϕ}) be small.

The solid black points in Figure 13 survive both of the above cuts, and exhibit a reasonably tight correlation between the two inclination estimators, consistent with their error distribution (dotted curves lines). The inclination errors in Figure 14 are comparable for the two methods in the 30°–40° range; inverse TF errors become substantially better at smaller inclinations. Interestingly, the most significant outlier of this exclusive sample is PGC 26140, which is an unusual galaxy hosting

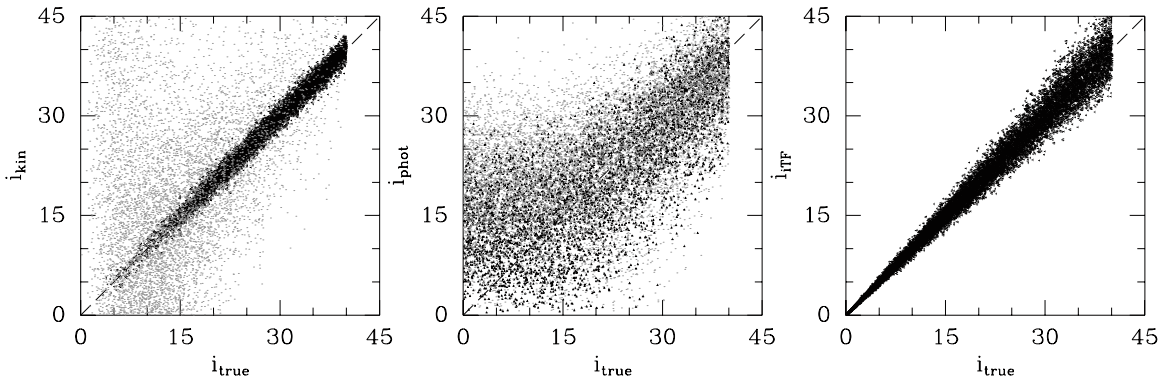


Figure 12. Results of Monte Carlo simulations of kinematic (left), photometric (center), and inverse TF inclinations (right). If we include our hypothesis that galaxies with sizable kinematic asymmetries (A_ϕ/v_{rot}) have kinematic inclination errors which are inconsistent with the χ^2 predicted confidence intervals, we find large scatter between the kinematic inclination and the true inclination. Most galaxies with inclinations less than $\sim 15^\circ$ will not meet our criteria of reliable kinematic inclinations (darker points). There is large scatter between the photometric and true inclinations, and a significant offset at low inclinations. The Monte Carlo model includes a distribution in the intrinsic ellipticity of galaxies. For galaxies with which are very nearly circular (darker points), the scatter is reduced somewhat and the offset decreases to lower inclinations. The scatter between the inverse TF and true inclinations depends primarily on the scatter in the TF relation. We are not including galaxies which may fall off TF in our simple model.

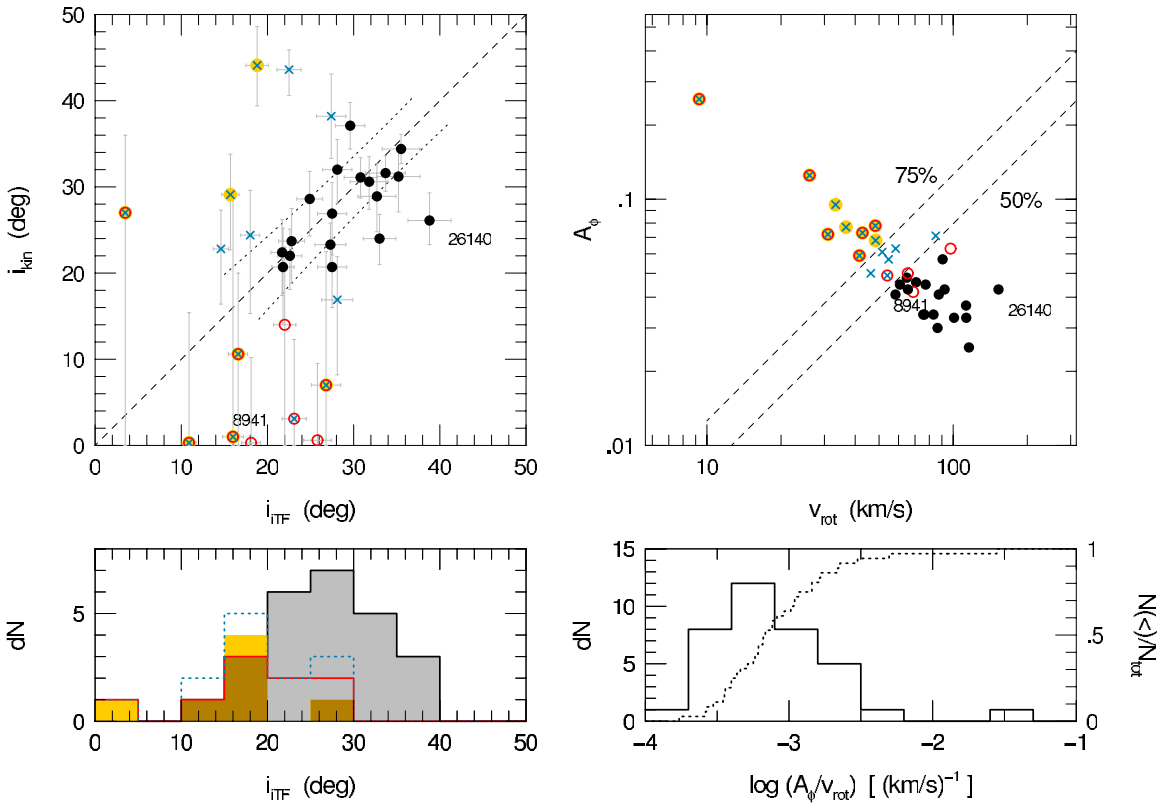


Figure 13. Comparison of kinematic and inverse Tully–Fisher inclinations (top left) for different subsamples selected on the basis of projected rotation speed (v_{rot}) and azimuthal asymmetry (A_ϕ). The R band is used for i_{TF} except in two cases where only the I band is available. Red open circles represent galaxies with non-zero projected velocity (v_{rot}) but kinematic inclinations consistent with zero at the 68% CL. Yellow filled circles represent objects in the highest quartile of A_ϕ/v_{rot} ; blue crosses represent objects with A_ϕ/v_{rot} above the median. The correlation between A_ϕ and v_{rot} , used to make these cuts, is shown in the top-right panel. The remaining filled black circles represent galaxies with the lowest values of A_ϕ/v_{rot} and kinematic inclinations inconsistent with zero. Dotted lines in the upper right panel give the expected 68% CL for the distribution of this subsample given the estimated errors in Figure 14. Two galaxies identified as AGN are labeled in upper panels. The distribution of subsamples with inverse Tully–Fisher inclination is given in the bottom-left histogram. The distribution in A_ϕ/v_{rot} for the entire sample is given in the bottom-right histogram.

(A color version of this figure is available in the online journal.)

an active galactic nucleus (AGN; DensePak spectra reveal broad-line emission in its center, it is an unusually strong radio-continuum source, yet has no neutral-hydrogen detection; Andersen et al. 2006). It is quite plausible that in this case the inverse TF inclination is systematically in error.

For our Monte Carlo simulation of galaxies with true inclinations spread uniformly between 0° and 40° , we used the absorption magnitudes (including measurement error and TF scatter) to generate v_{rot} values. We assume A_ϕ is normally distributed with the same properties of the DensePak sample and then kinematic inclination errors are generated proportional to A_ϕ/v_{rot} , as shown in Figure 13. If $A_\phi/v_{\text{rot}} > 8 \times 10^{-4}$ km $^{-1}$ s, we assume the kinematic fit breaks down and the kinematic inclination error becomes very large. In Figure 12, we emphasize

that magnitudes (including measurement error and TF scatter) to generate v_{rot} values. We assume A_ϕ is normally distributed with the same properties of the DensePak sample and then kinematic inclination errors are generated proportional to A_ϕ/v_{rot} , as shown in Figure 13. If $A_\phi/v_{\text{rot}} > 8 \times 10^{-4}$ km $^{-1}$ s, we assume the kinematic fit breaks down and the kinematic inclination error becomes very large. In Figure 12, we emphasize

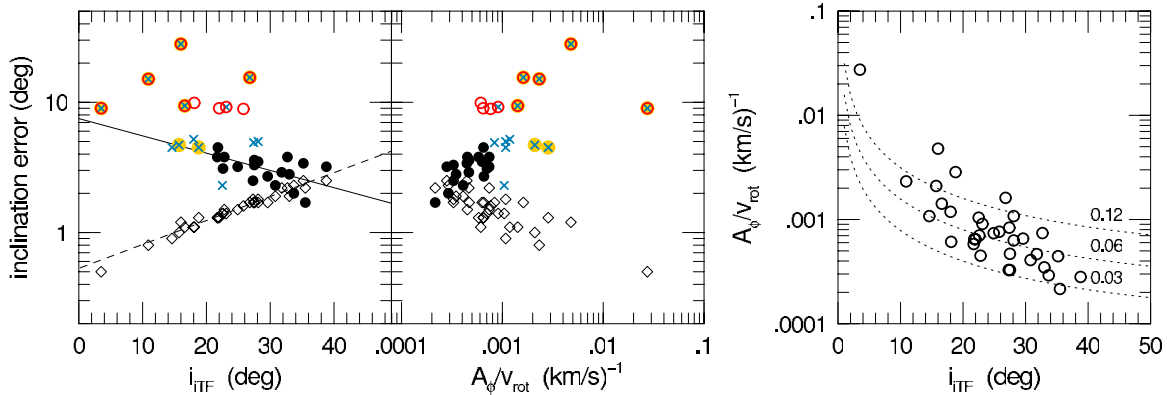


Figure 14. Trends of inclination errors and A_ϕ/v_{rot} vs. inclination. Symbols in left and middle panels are the same as in Figure 13 and represent estimated errors in kinematic inclinations; diamonds represent estimated inclination errors for the inverse Tully–Fisher method (R band) for the entire sample. Solid and dashed lines in the rightmost panel are estimates of trends in errors with inclination used in Figure 13. Circles in the right panel represent the full sample. Dotted curves illustrate the trend in A_ϕ/v_{rot} vs. inclination for a circular speed of 220 km s^{-1} and representative values of A_ϕ (labeled).

(A color version of this figure is available in the online journal.)

those points with $A_\phi/v_{\text{rot}} < 8 \times 10^{-4} \text{ km s}^{-1}$. For these simulated galaxies with low asymmetry, there is a generally good agreement between kinematic and true inclination angle. The fraction of galaxies with good inclinations (low asymmetries) increases with inclination because of the corresponding average increase in v_{rot} . Very few galaxies with inclinations less than 15° have low values of A_ϕ/v_{rot} . Galaxies with large asymmetries do not show a correlation between the kinematic and true inclinations. This is by construction in this Monte Carlo model, but it mirrors the agreement we see in our sample between inverse TF and kinematic inclinations.

In summary, we have found two fair performance estimators for kinematic inclinations (the estimators depend only on kinematic information). This allows us to cull a sample with robust inclination estimates even in the absence of inverse Tully–Fisher methods. For our sample, all galaxies with inclinations above 30° have good kinematic inclination estimates with errors comparable to inverse Tully–Fisher estimates. The success rate declines to 60% for $20^\circ < i < 30^\circ$, and zero below this range (Figure 13). This is a significant improvement over early generations of kinematic inclination estimates from tilted rings which become severely limited below 40° (e.g., Begeman 1989). Figure 14 can be used to estimate the performance of kinematic inclinations for other samples. At a given inclination, A_ϕ/v_{rot} depends on both the relative kinematic asymmetry as well as the circular speed; kinematic inclinations will work best for massive, kinematically regular systems.

5.3.1. On the Suitability of the Pseudo-isothermal Model

Having established a subsample of galaxies with minimal kinematic asymmetries for which we believe the kinematic inclinations should be accurate and precise, we explore whether using v_{PISO} in the formulation of the inverse TF inclination is reasonable. While we found the pseudo-isothermal sphere model produces a reasonably good fit to the inner part of the rotation curves, in accordance with other studies (e.g., van Eymeren et al. 2009; Oh et al. 2011), the parameter v_{PISO} derived from the pseudo-isothermal sphere model is systematically greater than v_{rot} derived from the empirical tanh rotation-curve model. If we use these two asymptotic model velocities to represent the flat speed of the rotation curve, inverse TF inclinations derived from the pseudo-isothermal sphere will be systematically greater than the tanh model inverse

TF inclinations (Figure 15). Indeed, these pseudo-isothermal sphere inverse TF inclinations are in disagreement with the subsample of galaxies with $A_\phi/v_{\text{rot}} < 8 \times 10^{-4} \text{ km s}^{-1}$ and kinematic inclinations inconsistent with zero. This, along with the fact that v_{PISO} is often times larger than the H I integrated line width, suggests that while the pseudo-isothermal sphere model does produce reasonable fits to the inner parts of galaxies in this sample, the implied asymptotic rotation speed is not physically meaningful.

5.4. Photometric Inclinations

Finally, we have also compared our inverse Tully–Fisher and kinematic inclinations to inclinations derived from the photometry. Photometric inclinations were derived by assuming $\cos i_{\text{phot}} = b/a$.⁶ We measured b/a of the isophotal axis ratios in the manner described in Andersen et al. (2001), which tries to account for the variation in isophote ellipticity with radius. In summary, after examining the isophote fits, we defined an inner and outer radii (r_{inner} and r_{outer} ; see Table 2) in which the ellipticity and position angle of the isophotes was relatively constant and measured ellipticity within this radius (Table 2). The inferred photometric inclinations are given in Table 4. Measurements were made in I band, or, when I -band data were unavailable, in the R band.

When we compare the photometric inclinations to inverse Tully–Fisher inclinations and kinematic inclinations (Figure 16), one sees a strong correlation in general.⁷ This despite the fact that a number of factors, such as the influence of spiral structure, warps (the ellipticity is often measured at several scale lengths), and perhaps the intrinsic ellipticity of the disks, would decrease our confidence in the accuracy of the axis ratio measurement. Due to these factors, we suspect that the formal precision of the axis ratio measurements underestimates the uncertainty in the inferred photometric inclinations. However, we also note that if one creates a weighted mean of

⁶ It is reasonable to neglect the disk thickness in this calculation because the galaxies in this sample are close to face-on and the measurement is made in the outer part of the disk where the thickness is minimal.

⁷ Only two galaxies, PGC 28401 and PGC 32091, have wildly different photometric versus kinematic inclinations. Both these galaxies are very nearly face-on. The difference can probably be attributed at least partly to the great difficulty of measuring an axis ratio near unity. All errors, both random and systematic, will act to decrease the axis ratio measurement, thereby artificially increasing the photometric inclination.

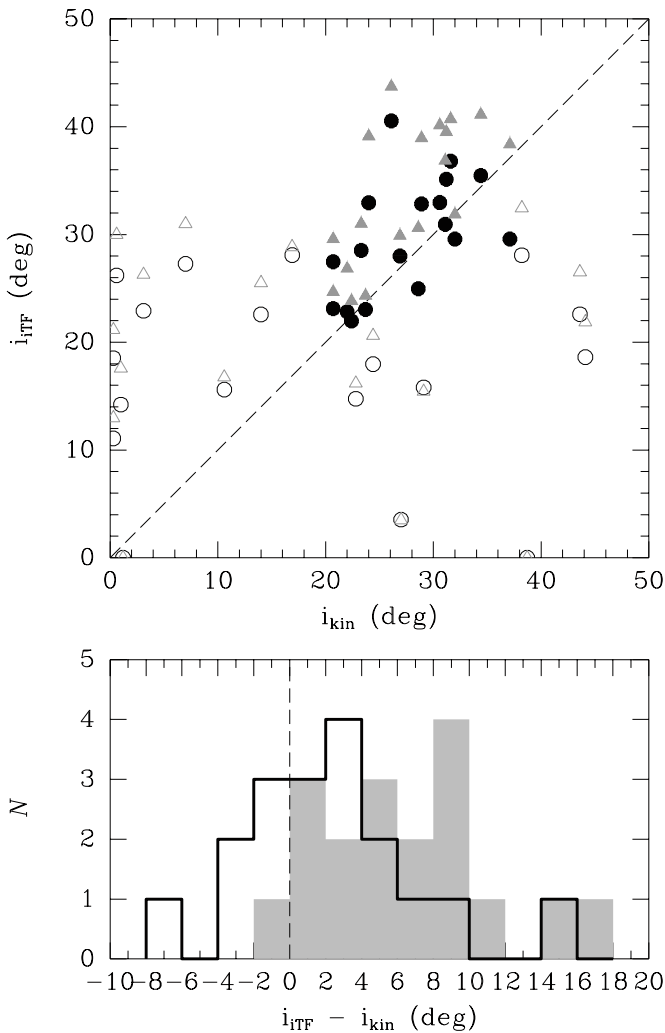


Figure 15. Top panel: comparison of kinematic vs. inverse TF inclinations calculated making use of the empirical tanh asymptotic velocity, v_{rot} , (dark circles) or the pseudo-isothermal model asymptotic velocity, v_{pISO} , (gray triangles). Points denoted with open symbols have kinematic inclinations consistent with zero or significant kinematic asymmetries, as characterized by $A_\phi/v_{\text{rot}} > 8 \times 10^{-4} \text{ km}^{-1} \text{ s}$. Bottom panel: histogram of the differences between kinematic and inverse TF inclinations as calculated using v_{rot} (heavy line) or v_{pISO} (shaded region) for those galaxies with kinematic inclinations inconsistent with zero and $A_\phi/v_{\text{rot}} < 8 \times 10^{-4} \text{ km}^{-1} \text{ s}$ (black points in top panel). There is a significant offset in the inclination differences when using v_{pISO} which we believe indicates that the pseudo-isothermal model is predicting asymptotic velocities which are greater than the true “flat” rotation speed.

the photometric and kinematic inclination, this mean is more highly correlated with the inverse TF inclination than either of the measures are on their own.

Again, we simulated the errors on the photometric inclination from our Monte Carlo sample of galaxies with a uniform distribution of inclinations between 0° and 40° . We assumed the error on the axis ratio measurement was 0.03, matching the mean errors quoted for our sample. We also assumed a normally distributed 5% error on the intrinsic ellipticity of the disk. Again, this ellipticity could be due to weak spiral arm structure, warps or an intrinsic ellipticity of the disk. This ellipticity is assumed to be randomly distributed in azimuth with respect to the inclination axis. At low intrinsic inclinations, this random ellipticity will manifest itself as increasingly large photometric inclination errors; an inclined ellipse is unlikely to appear circular. Under these assumptions, the scatter between photometric and true inclinations is large and there

is a systematic error for inclinations less than $\cos 0.95 \sim 20^\circ$ (Figure 12). If one only selects galaxies with intrinsic ellipticities less than 2%, the offset at low inclination sets in at $\cos 0.98 \sim 10^\circ$, and the scatter decreases somewhat.

5.5. Scaling Relations

As an initial demonstration of the accuracy of kinematic inclinations, Andersen & Bershady (2003) demonstrated that a TF relation could be established for the galaxies in the current analysis. This nearly face-on TF relation for these galaxies is consistent with larger TF samples of more inclined galaxies. (e.g., Courteau 1997; Verheijen 2001). Here, we explore two other scaling relations between rotation speed, disk scale length, and the rising scale of the rotation curve (h_{rot}). This is worthwhile as an additional check on the accuracy of kinematic inclinations and because of the difference in projection of our sample compared to most other disk galaxy studies. In particular, it can address possible systematic effects of inclination on estimated scale lengths.

We have measured both photometric and kinematic scale lengths (exponential scale length h_r in Table 2 and tanh characteristic scale h_{rot} in Table 3, respectively). Photometric disk scale lengths (h_r) and central surface brightnesses (μ_0) were taken from bulge-disk decompositions of the 2D images. We minimized χ^2 using the downhill simplex method for our bulge and disk model with respect to imaging covering 4 arcmin^2 centered on each galaxy, with point sources masked. After χ^2 minimization, we found the strongest residuals resulted from spiral structure. Therefore, in Table 2 we report the I -band disk parameters to try to minimize contamination from spiral structure. We did not convolve our models with the seeing, so in general our bulge parameters underestimate the bulge surface brightness and overestimate the bulge scale length, but here we are only concerned with the disk parameters which are relatively insensitive to the seeing. Disk fitting results were consistent with those obtained from the one-dimensional surface brightness profiles using the IRAF *nfit1d* routine.

Both the photometric and kinematic scale lengths correlate with $V_{\text{rot}} = v_{\text{rot}} / \sin i_{\text{TF}}$.⁸ Figure 17 shows the relationship we find between h_r and V_{rot} is in excellent agreement with both the slope and scatter reported in Courteau et al. (2007); $h_r \propto V_{\text{rot}}^{1.1}$ with a scatter of $\sigma_{\ln h_r} = 0.38$; galaxies which rotate faster (and are more luminous) are also larger. Figure 17 also shows that more rapidly rotating galaxies have rotation curves which rise more rapidly relative to their disk scale length. This trend is well known (Sofue & Rubin 2001 and references therein), and well-quantified by Cantinella et al. (2006) for more inclined galaxies ($i > 30^\circ$) using a slightly more complex rotation-curve model. Our results agree qualitatively with those of Cantinella et al. (2006).

Interestingly, the relation we observe between the ratio h_{rot}/h_r and V_{rot} in Figure 17 does not come naturally out of the two individual relations between h_r and h_{rot} and V_{rot} . This indicates there are additional parameters determining these scaling relations. Two additional parameters which are undoubtedly important are the disk surface brightness (μ_0) and the bulge–disk ratio, which we parameterize with the concentration index C (Section 2.2). Figure 18 shows residuals of the h_r versus V_{rot} and h_{rot} versus V_{rot} relations from Figure 17 versus μ_0 and C , respectively. It is sensible that galaxies with

⁸ The characteristic scale of the pseudo-isothermal sphere model correlates with V_{rot} as well.

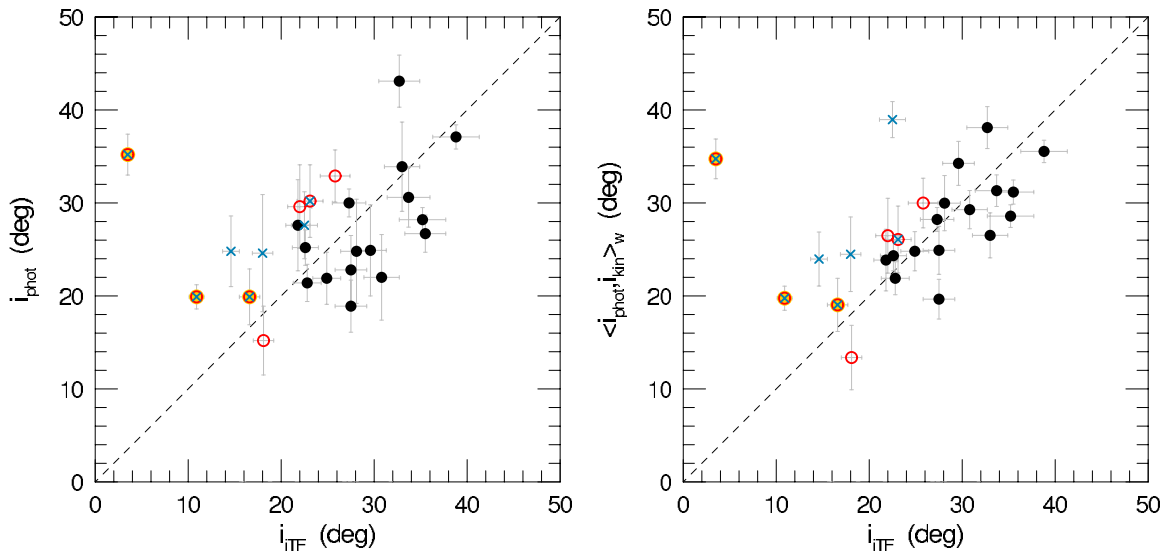


Figure 16. Left panel: comparison of inverse TF inclinations vs. photometric inclinations. Points marked with blue crosses have large kinematic asymmetries ($A_\phi/v_{\text{rot}} > 8 \times 10^{-4} \text{ km s}^{-1}$). Points with red circles have kinematic inclinations consistent with zero. Right panel: comparison of inverse TF inclinations to the weighted mean of the kinematic and photometric inclinations. Points are marked in the same manner as those in the left panel. Combining photometric and kinematic inclination information produces a better surrogate for the inverse TF relation than either of the measures individually.

(A color version of this figure is available in the online journal.)

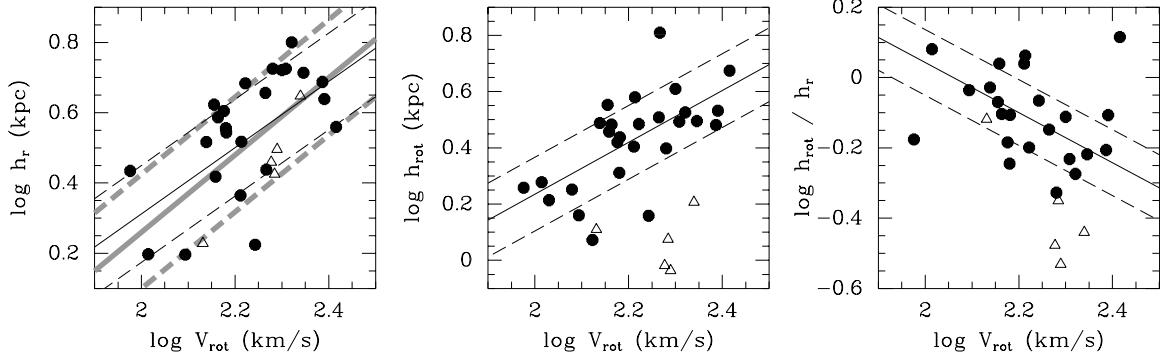


Figure 17. Left panel: $\log V_{\text{rot}}$ vs. $\log h_r$ in kpc. The heavy gray line is the relation between scale length (from I -band measurements) and rotation speed reported by Courteau et al. (2007; slope 1.1, $\sigma_{\ln h_R} = 0.38$) which is consistent with the relation measured from our data (thin black line). The dashed lines are the 68% error bars from Courteau et al. (2007; gray lines) and our data (black lines). In all three panels, the points marked with open triangles have kinematic scale lengths, $h_{\text{rot}} < 4''$ (one fiber diameter). Central panel: $\log V_{\text{rot}}$ vs. $\log h_{\text{rot}}$ in kpc. Right panel: $\log V_{\text{rot}}$ vs. $\log (h_{\text{rot}}/h_r)$. An apparent relation between rotation speed and the ratio of kinematic to photometric scale length is marked. Galaxies with relatively small h_{rot} (fast risers) were faster rotators.

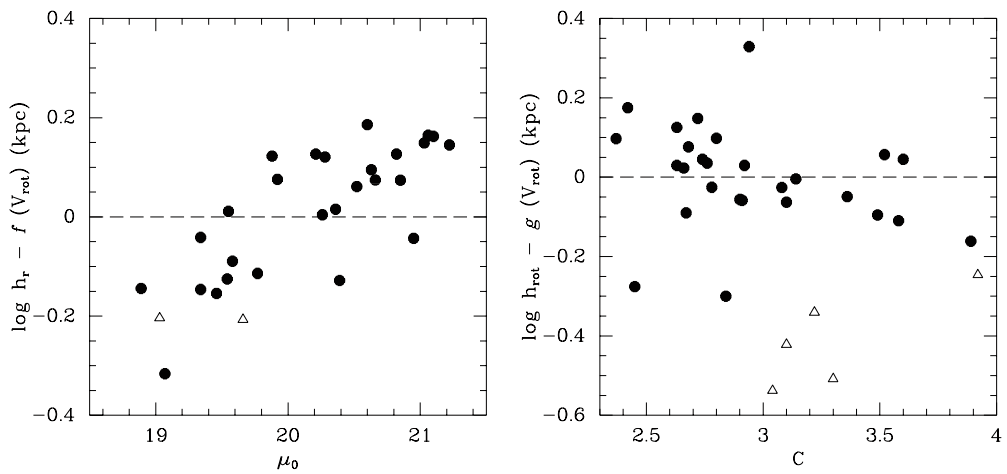


Figure 18. Left panel: residuals of the $\log h_r$ vs. V_{rot} relation from Figure 17 vs. the central disk surface brightness μ_0 . Right panel: residuals of the $\log h_{\text{rot}}$ vs. V_{rot} relation from Figure 17 vs. concentration index C . Galaxies with $h_{\text{rot}} < 4''$ (one fiber diameter) are marked with open triangles. In both panels, there is a clear relation between the residual in the relation and either surface brightness or concentration index.

higher surface brightnesses have relatively shorter photometric scale lengths than predicted by V_{rot} alone; for galaxies obeying the Tully–Fisher relation with relatively small bulge–disk ratios, $M \propto \log V_{\text{rot}} \propto 10^{-0.4\mu_0} h_r^2$. Likewise, it is not surprising that galaxies that are more concentrated have faster rising rotation curves. A similar behavior was reported by Swaters et al. (2009) for late-type galaxies.

In contrast to these correlations between scaling-relation residuals and other properties of the light profile, residuals in h_r versus V_{rot} appear to be uncorrelated with C , and the same is true for h_{rot} residuals with respect to μ_0 . Hence, it would seem plausible that μ_0 and C might explain the relation between h_{rot}/h_r and V_{rot} , yet our data do not lead to a definitive conclusion. Specifically, residuals of h_{rot}/h_r versus V_{rot} have only weak correlations with either μ_0 or C . This may be a result of a weak correlation between μ_0 and C themselves. Resolving this puzzle merits future exploration.

6. SUMMARY

We gathered H α emission-line data for 39 nearly face-on spiral galaxies with the DensePak IFU on WIYN, as well as flux-calibrated R - and I -band images from several observatories. From the spectrally resolved emission-line data we derived relative fluxes, widths, centroids, and mean continuum levels. Using the line centroids, we created H α velocity-field maps and rotation-curve diagrams. The high-quality DensePak velocity fields clearly showed rotation and the position angle of the kinematic major axis for galaxies with *projected* rotation speeds as low as 50 km s $^{-1}$. We also presented surface brightness profiles produced from maps of the spectral continuum levels; these compared favorably to the surface brightness profiles measured in the R band. The comparison indicates DensePak observations can be used to measure equivalent widths and absorption line features.

We successfully fit the observed 2D velocity fields with a simple hyperbolic tangent velocity-field model. From these fits kinematic inclinations, position angles, rotation speeds, and disk rotation scale lengths were derived for 36 of the 39 sample galaxies. All sample galaxies have inclinations less than 45°, and projected rotation speeds less than 150 km s $^{-1}$. We independently verified that the spatial registration of multiple IFU pointings were consistent based on our kinematic model fitting and constraints from comparison between the radial profiles of spectra continuum to broadband surface photometry.

We detected kinematic asymmetries in several galaxies through different means. Eight galaxies exhibited significant rotation-curve asymmetries ($A_{\text{RC}} \geq 0.1$), and five of these galaxies also showed significant velocity-field asymmetries ($A_{\phi} \geq 0.06$). An additional three galaxies showed only velocity-field asymmetries. Different kinematic asymmetries correlate well with each but not with global line-profile asymmetries measured in Andersen & Bershady (2009). The lack of a relation between purely kinematic and line-shape asymmetry parameters is perhaps surprising; many of the theories which describe physical mechanisms behind disk asymmetry would excite both kinematic modes and the distribution of gas. More work is needed before the physical basis for disk asymmetry can be understood, but our present analysis reinforces the notion that line-width asymmetries are largely driven by asymmetric distributions of ionized gas and not kinematic asymmetries.

The key to measuring disk ellipticity and creating a “face-on” TF relation is accurate and precise measures of *kinematic* inclination angles at low inclination. We believe that the precision

of kinematic inclinations derived from H α velocity fields can be significantly increased at low inclinations by abandoning the tilted-ring fitting method and adopting our single, inclined-disk method. The prime motivation for using tilted-ring fits does not apply to our sample; we are not detecting H α at radii where warping is of concern. Specifically, we do not observe large position angle twists for our sample. Hence, a single-disk model can be employed which increases precision because there is strong covariance between radius and inclination especially in radial regions where the rotation curve is not flat. We also weight all data equally, in contrast to tilted-ring fits which ignore data in regions which are most sensitive to inclination differences in nearly face-on galaxies. This gives us further gains in precision over the traditional methods used with H I velocity fields. H α velocity fields also have advantages over stellar velocity fields. One may expect that stellar velocity fields would be subject to less random motion and asymmetries induced by spiral arms than H α velocity fields, but in general, it is found that stellar rotation curves rise more slowly than H α velocity fields and therefore the stellar velocity fields appear to be more like a solid body and hence the sensitivity to changes in inclination is reduced (cf. Westfall et al. 2011; Martinsson et al. 2013).

We tested the accuracy of our kinematic inclinations by comparing them to inclination estimates from inverting the Tully–Fisher relation and from disk axis ratios. The agreement between so-called inverse Tully–Fisher inclinations and kinematic inclinations is good, and consistent with estimated errors provided two conditions are met: (1) the kinematic inclination is non-zero at the 68% CL or above when projected rotation is visibly evident, or (2) the ratio of the relative azimuthal kinematic asymmetry (A_{ϕ}) to the projected rotation speed (v_{rot}) is $A_{\phi}/v_{\text{rot}} < 8 \times 10^{-4}$ km $^{-1}$ s. Both conditions probe whether the amplitude of smooth, iso-velocity curvature due to inclination is sufficiently large relative to random noise and non-circular motions. With this culling, we find kinematic inclination estimates using H α kinematic data from DensePak in this survey are accurate down to 20°, with a precision of better than 5°. Above 30°, the precision of kinematic inclinations is comparable, or superior to inverse Tully–Fisher inclination estimates.

Finally, we measured relations between the intrinsic photometric and kinematic scale lengths and the deprojected rotation speed. We clearly see that galaxies with faster rotating disks have larger disks (consistent with a scaling relation already established for more inclined systems), but also have rotation curves that rise more quickly relative to their photometric disk scale lengths. This trend in rotation-curve shape is indicative of increased light concentration in more massive disks systems which to first order is independent of disk surface brightness.

Research was supported by NSFAST-1009491. M.A.B. acknowledges support from the Wisconsin Alumni Research Foundation Vilas Fellowship and the University of Wisconsin College of Letters and Science Ciriacks Faculty Fellowship, and thanks to the NRC Herzberg Institute of Astrophysics for their hospitality during a portion of this research effort.

APPENDIX

OPTICAL IMAGING OBSERVATIONS

The properties of the imaging cameras and telescopes used for acquiring the photometry described in Section 2.2 are summarized in Table 5. We chose exposure times which yielded images with sufficient signal to noise to measure axis ratios

Table 5
Instrument Properties

Observatory	Telescope	Instrument	F#	Scale ($''$ pixel $^{-1}$)	Field of View (arcmin 2)	Read Noise (e^-)	Gain (e^- ADU $^{-1}$)	Overscan Columns	Zero Points ($e^- m^{-2} s^{-1}$)	
									R band	I band
WIYN	WIYN 3.5 m	S2KB	6.3	0.195	6.7×6.7	8.0	2.8	32	23.65	23.11
WIYN	WIYN 3.5 m	MiniMo	6.3	0.141	9.5×9.5	5.4	1.3	50	23.63	22.91
KPNO	2.1 m	T2KA	7.5	0.305	10.4×10.4	4.0	3.6	30	23.90	23.21
McDonald	2.7 m	IGI	8.8	0.57	7×7	4.1	2.5	16	22.17	21.57

Table 6
Observing Log

PGC	R band						I band					
	Instrument	U.T. Date (mm/dd/yy)	Exposure (s)	Q	Seeing (arcsec)	Total Magnitude	Instrument	U.T. date (mm/dd/yy)	Exposure (s)	Q	Seeing (arcsec)	Total Magnitude
02162	MiniMo	10/16/00	450	1	0.8	14.08 ± 0.02	MiniMo	10/16/00	450	1	0.8	13.54 ± 0.02
03512	MiniMo	10/17/00	450	1	0.7	13.35 ± 0.02	MiniMo	10/17/00	450	1	0.7	12.76 ± 0.02
05345	T2KA	01/21/01	1000	1	0.8	14.16 ± 0.04	T2KA	01/20/01	1500	1	0.8	13.76 ± 0.05
05673	T2KA	01/21/01	600	1	0.8	13.30 ± 0.04	T2KA	01/20/01	1500	1	0.8	12.76 ± 0.05
06855	T2KA	01/20/01	1200	1	0.8	13.79 ± 0.05	T2KA	01/20/01	1200	1	0.8	13.21 ± 0.05
07826	T2KA	01/21/01	500	1	1.2	13.58 ± 0.04	MiniMo	11/19/00	450	2	2.2	12.98 ± 0.05
08941	T2KA	01/21/01	1000	1	1.2	13.44 ± 0.04	S2KB	09/05/99	600	2	0.9	12.86 ± 0.05
14564	T2KA	01/21/01	800	1	0.9	12.66 ± 0.04	S2KB	09/06/99	450	2	0.9	12.10 ± 0.05
15531	T2KA	01/21/01	900	1	1.1	13.85 ± 0.04	S2KB	09/06/99	450	2	0.9	13.32 ± 0.05
16274	T2KA	01/22/01	400	3	1.2	13.67 ± 0.04	T2KA	01/22/01	400	3	1.2	12.92 ± 0.05
19767	T2KA	01/21/01	400	1	1.0	14.06 ± 0.04	T2KA	01/21/01	400	1	1.0	13.39 ± 0.05
20938	T2KA	01/21/01	400	1	1.0	14.25 ± 0.04	T2KA	01/20/01	1200	2	0.8	...
23333	T2KA	01/22/01	1800	4	1.2	13.55 ± 0.05	MiniMo	02/08/00	450	4	1.1	...
23598	T2KA	01/21/01	1200	1	1.0	13.67 ± 0.04	S2KB	05/12/99	750	2	0.7	13.07 ± 0.04
23913	IGI/TK4	05/19/99	800	3	1.6	13.71 ± 0.05	IGI/TK4	05/21/99	600	2	2.0	13.31 ± 0.05
24788	T2KA	01/21/01	400	1	1.0	13.59 ± 0.04	T2KA	01/20/01	1200	2	0.7	13.11 ± 0.05
26140	T2KA	01/21/01	400	1	1.0	12.74 ± 0.04	S2KB	05/11/99	300	2	1.4	12.28 ± 0.05
26517	T2KA	01/21/01	1200	1	1.0	14.54 ± 0.02	T2KA	01/21/01	400	1	1.0	14.18 ± 0.02
27792	MiniMo	03/04/00	450	3	1.6	...
28310	T2KA	01/20/01	1200	3	0.6	...	S2KB	05/11/99	1200	2	1.4	13.86 ± 0.05
28401	MiniMo	11/19/00	450	2	1.5	13.12 ± 0.05	MiniMo	11/19/00	450	2	1.5	12.42 ± 0.05
31159	IGI/TK4	05/20/99	600	3	1.8	...	S2KB	05/11/99	450	2	1.0	13.00 ± 0.05
32091	MiniMo	03/04/00	450	3	1.6	...
32638	T2KA	01/21/01	1200	1	1.0	13.11 ± 0.04	T2KA	01/21/01	400	1	1.0	12.57 ± 0.04
33465	T2KA	01/21/01	1000	1	1.0	12.51 ± 0.04	MiniMo	03/04/00	450	4	1.3	...
36925	IGI/TK4	05/21/99	600	4	2.0	13.26 ± 0.10	S2KB	05/11/99	600	2	1.4	12.61 ± 0.05
38268	T2KA	01/21/01	1200	1	0.9	13.51 ± 0.02	T2KA	01/21/01	1200	1	0.9	13.03 ± 0.02
38908	IGI/TK4	05/19/99	600	3	1.8	13.28 ± 0.05	S2KB	05/11/99	450	2	1.1	13.00 ± 0.05
39728	T2KA	01/21/01	1200	1	0.9	12.46 ± 0.04
46767	IGI/TK4	05/19/99	600	3	1.6	12.56 ± 0.10	S2KB	05/11/99	300	2	1.1	12.15 ± 0.05
49906	IGI/TK4	05/19/99	600	3	1.6	13.88 ± 0.10	S2KB	05/11/99	450	2	1.4	13.36 ± 0.05
55750	IGI/TK4	05/19/99	462	3	1.8	13.58 ± 0.10	S2KB	05/11/99	450	2	1.9	12.41 ± 0.05
56010	IGI/TK4	05/19/99	562	3	1.8	15.30 ± 0.10	S2KB	05/11/99	750	2	1.8	13.74 ± 0.05
57931	T2KA	0/121/01	900	1	0.9	13.86 ± 0.04	IGI/TK4	05/20/99	800	2	2.3	13.69 ± 0.05
58410	IGI/TK4	05/19/99	600	3	1.6	13.54 ± 0.10	IGI/TK4	05/19/99	506	3	1.6	13.49 ± 0.05
70962	MiniMo	10/16/00	450	1	0.65	13.16 ± 0.02	MiniMo	10/16/00	450	1	0.45	12.59 ± 0.02
71106	MiniMo	10/16/00	450	1	0.35	12.78 ± 0.02	MiniMo	10/16/00	450	1	0.35	12.16 ± 0.02
72144	MiniMo	10/16/00	450	1	0.6	14.80 ± 0.02	MiniMo	10/16/00	450	1	0.6	14.12 ± 0.02
72453	MiniMo	10/16/00	450	1	0.8	13.74 ± 0.02	MiniMo	10/16/00	450	1	0.7	13.10 ± 0.02

Notes. “Instrument” designation is for the WIYN 3.5 m telescope (MiniMo and S2KB), the KPNO 2.1 m (T2KA), and the McDonald 2.7 m (IGI/TK4). Q is the photometric zero-point uncertainty, as defined in the text. The seeing is given for the FWHM.

and position angles out to ~ 4.5 scale lengths in Freeman disks; limiting surface brightnesses for our images were $\mu_R = 25.5$ mag arcsec $^{-2}$. Typical exposure times were 1000 s at the KPNO 2.1 m telescope, 600 s at the McDonald 2.7 m telescope, and 450 s at the WIYN 3.5 m telescope.

For each night of data, we collected a complete set of bias frames taken at the beginning and ending of each night along

with dome flats typically taken during twilight hours. Standard stars were observed on four photometric nights. We collected R -band images for 37 of the 39 galaxies and imaged 38 of the sample galaxies in the I band. Repeat observations were used to internally calibrate photometry from runs which were probably photometric but during which no standard stars were observed. An observing log of objects, telescopes,

instruments, filters, exposure times, seeing, quality, and total magnitudes can be found in Table 6.

A.1. Image Processing

We used standard IRAF tasks to process images for overscan correction, bias subtraction, and flat-fielding. The standard IRAF cosmic-ray cleaning task was augmented using information from neighboring pixels, thus enhancing the cleaning of extended cosmic-ray hits (and detector flaws). All *I*-band images were fringe corrected. We created master fringe frames by masking sources and combining all long exposures taken in a night, scaling by the exposure time. The high spatial frequency fringe patterns remained constant from night to night, allowing us to combine fringe frames from different nights. The IRAF *ccddproc* routine scaled this master fringe frame to image frames and subtracted the fringe pattern from data. Once individual data frames were fully processed, the sky background was calculated using an iteratively clipped mean and subtracted from all frames. Offsets between multiple target exposures were applied and frames were combined, yielding fully reduced and combined images in *R* and *I* bands for all of our imaging observations.

A.2. Total Magnitudes and Photometric Calibration

We verified that the curves of growth of the integrated light profile reached asymptotic values at large radii, indicating a satisfactory background subtraction. Because the signal-to-noise ratio was so high we have the luxury of using those asymptotic counts from the curves of growth to calculate total *R*- and *I*-band magnitudes after we set photometric zero points.

To calibrate magnitude zero points for our observations, we used Landolt (1983) standards observed during four photometric nights.⁹ Air mass corrections have not been applied to these data but they should be small (less than 0.1 mag) as all objects were observed with airmasses less than 1.5. In addition to these directly calibrated data, there were several runs which had estimated photometric errors under 0.05 mag, but for which no standard stars were observed.¹⁰ After correcting asymptotic counts for gain, telescope apertures, and exposure times, we calculated an internal boot-strapped calibration for these runs based on repeat observations of targets taken during directly calibrated runs. The data from the indirectly calibrated runs had magnitude zero-point errors estimated to be less than 0.05 based on both repeat observations taken during directly calibrated runs and exposure-to-exposure variations. We used our internal calibration to set magnitude zero points (for fluxes measured in $e^- m^{-2} s$) for all instrument and telescope combinations (Table 5). We also measured magnitudes for some galaxies from the McDonald 0599 run even though photometric errors were large because we could directly calibrate these data with observed Landolt standard stars during this run. In Table 6, we assign a photometric zero-point uncertainty flag, *Q*, determined by (1) frame-to-frame variations in the raw data for selected field stars and (2) comparison of photometry from run to run. The flag *Q* designates these meanings: *Q* = 1 (photometric conditions); *Q* = 2 (photometric errors less than 0.05 mag); *Q* = 3 (photometric errors between 0.05 and 0.10 mag); *Q* = 4 (photometric errors >0.1 mag).

⁹ Dates (mm/dd/yy) include 1/20/01 and 1/21/01 at the KPNO 2.1 m telescope and 1016/01 and 10/17/01 at the WIYN telescope.

¹⁰ These included five runs on the WIYN 3.5 m telescope with UT dates of (mm/yy) 05/98, 05/99, 09/99, 11/00, and 12/00.

REFERENCES

- Andersen, D. R., & Bershady, M. A. 2003, *ApJL*, 599, L79
 Andersen, D. R., & Bershady, M. A. 2009, *ApJ*, 700, 1626
 Andersen, D. R., Bershady, M. A., Sparke, L., Gallagher, J., & Wilcots, E. 2001, *ApJL*, 551, L131
 Andersen, D. R., Bershady, M. A., Sparke, L. S., et al. 2006, *ApJS*, 166, 505
 Andersen, D. R., Walcher, C. J., Böker, T., et al. 2008, *ApJ*, 688, 990
 Angiras, R. A., Jog, C. J., Dwarakanath, K. S., & Verheijen, M. A. W. 2007, *MNRAS*, 378, 276
 Bagetakis, I., Brinks, E., Walter, F., et al. 2011, *AJ*, 141, 23
 Baldwin, J. E., Lynden-Bell, D., & Sancisi, R. 1980, *MNRAS*, 193, 313
 Beauvais, C., & Bothun, G. 1999, *ApJS*, 125, 99
 Begeman, K. G. 1989, *A&A*, 223, 47
 Bershady, M. A. 1995, *AJ*, 109, 87
 Bershady, M. A., Andersen, D. R., Harker, J., et al. 2004, *PASP*, 116, 565
 Bershady, M. A., Andersen, D. R., Verheijen, M. A. W., et al. 2005, *ApJS*, 156, 311
 Bershady, M. A., Jangren, A., & Conselice, C. J. 2000, *AJ*, 119, 2645
 Bershady, M. A., Verheijen, M. A. W., Swaters, R. A., et al. 2010a, *ApJ*, 716, 198
 Bershady, M. A., Verheijen, M. A. W., Westfall, K. B., et al. 2010b, *ApJ*, 716, 234
 Bosma, A. 1981, *AJ*, 86, 1825
 Briggs, F. H. 1990, *ApJ*, 352, 15
 Cantinella, B., Giovanelli, R., & Haynes, M. P. 2006, *ApJ*, 640, 751
 Chemin, L., Balkowski, C., Cayatte, V., et al. 2006, *MNRAS*, 366, 812
 Christlein, D., Zaritsky, D., & Bland-Hawthorn, J. 2010, *MNRAS*, 405, 2549
 Courteau, S. 1997, *AJ*, 114, 2402
 Courteau, S., Dutton, A. A., van den Bosch, F. C., et al. 2007, *ApJ*, 671, 203
 Cousins, A. W. J. 1978, *MNSSA*, 37, 8
 Dale, D. A., Giovanelli, R., Haynes, M. P., et al. 2001, *AJ*, 121, 1886
 de Blok, W. J. G., & McGaugh, S. S. 1997, *MNRAS*, 290, 533
 de Blok, W. J. G., Walter, F., Brinks, E., et al. 2008, *AJ*, 136, 2648
 Dobbs, C. L., Burkert, A., & Pringle, J. E. 2011, *MNRAS*, 417, 1318
 Epinat, B., Amram, P., Marcelin, M., et al. 2008, *MNRAS*, 388, 500
 Espada, D., Verdes-Montenegro, L., Huchtmeier, W. K., et al. 2011, *A&A*, 532, 117
 Fathi, K., Beckman, J. E., Zurita, A., et al. 2007, *A&A*, 466, 905
 Förster Schreiber, N. M., Genzel, R., Bouche, N., et al. 2009, *ApJ*, 706, 1364
 Freeman, K. C. 1970, *AJ*, 160, 811
 Garrido, O., Marcelin, M., Amram, P., & Boulesteix, J. 2002, *A&A*, 387, 821
 Gilmore, G. F., King, I. R., & van der Kruit, P. C. 1990, in *The Milky Way as a Galaxy*, ed. R. Buser & I. R. King (Mill Valley, CA: University Science Books), 212
 Guijarro, A., Peletier, R. F., Battaner, E., et al. 2010, *A&A*, 519, 53
 Haynes, M. P., van Zee, L., Hogg, D. E., et al. 1998, *AJ*, 115, 62
 Jog, C. J. 1999, *ApJ*, 522, 661
 Kirby, E. M., Koribalski, B., Jerjen, H., & López-Sánchez, Á. 2012, *MNRAS*, 420, 2924
 Kornreich, D. A., Haynes, M. P., Lovelace, R. V. E., & van Zee, L. 2000, *AJ*, 120, 139
 Kranz, T., Slyz, A., & Rix, H.-W. 2001, *ApJ*, 562, 164
 Landolt, A. U. 1983, *AJ*, 88, 439
 Law, D. R., Steidel, C. C., Erb, D. K., et al. 2009, *ApJ*, 697, 2057
 Martinsson, T. M., Verheijen, M. A. W., Westfall, K. B., et al. 2013, *MNRAS*, submitted
 Metropolis, N., Rosenbluth, N., Rosenbluth, A., Teller, A., & Teller, E. 1953, *JChPh*, 21, 1087
 Neumayer, N., Walcher, C. J., Andersen, D., et al. 2011, *MNRAS*, 413, 1875
 Oh, S.-H., de Blok, W. J. G., Brinks, E., Walter, F., & Kennicutt, R. C., Jr. 2011, *AJ*, 141, 193
 Paturel, G., Petit, C., Prugniel, P., et al. 2003, *A&A*, 412, 45
 Persic, M., & Salucci, P. 1991, *ApJ*, 368, 60
 Press, W. H., Flannery, B. P., Teukolsky, S. A., & Vetterling, W. T. 1992, *Numerical Recipes* (Cambridge: Cambridge Univ. Press)
 Puech, M., Flores, H., Hammer, F., et al. 2008, *A&A*, 484, 173
 Richter, O.-G., & Sancisi, R. 1994, *A&A*, 290, L9
 Rix, H.-W., Guhatajura, P., Colless, M., & Ing, K. 1997, *MNRAS*, 285, 779
 Roberts, W. W. 1969, *ApJ*, 158, 123
 Rozas, M., Zurita, A., Beckman, J. E., & Pérez, D. 2000, *A&AS*, 142, 259
 Rubin, V. C., Ford, W. K., Jr., & Thonnard, N. 1980, *ApJ*, 238, 471
 Saha, K., de Jong, R., & Holwerda, B. 2009, *MNRAS*, 396, 409
 Schechtman-Rook, A., Bershady, M. A., & Wood, K. 2012, *ApJ*, 746, 70
 Schlegel, D. J., Finkbeiner, D. P., & David, M. 1998, *ApJ*, 500, 525
 Schoenmakers, R. H. M., Franx, M., & de Zeeuw, P. T. 1997, *MNRAS*, 292, 349

- Sellwood, J. A., & Sánchez, Z. R. 2010, *MNRAS*, **404**, 1733
- Shetty, R., Vogel, S. N., Ostriker, E. C., & Teuben, P. J. 2007, *ApJ*, **665**, 1138
- Simard, L. 1998, in ASP Conf. Ser. 145, Astronomical Data Analysis Software and Systems VII, ed. R. Albrecht, R. N. Hook, & H. A. Bushouse (San Francisco, CA: ASP), 108
- Sofue, Y., & Rubin, V. 2001, *ARA&A*, **39**, 137
- Swaters, R. A., Madore, B. F., van den Bosch, F. C., & Balcells, M. 2003, *ApJ*, **583**, 732
- Swaters, R. A., Sancisi, R., van Albada, T. S., & van der Hulst, J. M. 2009, *A&A*, **493**, 871
- Swaters, R. A., Schoenmakers, R. H. M., Sancisi, R., & van Albada, T. S. 1999, *MNRAS*, **304**, 330
- Tully, R. B., & Fisher, J. R. 1977, *A&A*, **54**, 661
- Tully, R. B., & Pierce, M. J. 2000, *ApJ*, **533**, 744
- van der Kruit, P. C. 2007, *A&A*, **466**, 883
- van der Kruit, P. C., & Allen, R. J. 1978, *ARA&A*, **16**, 103
- van Eymeren, J., Trachternach, C., Koribalski, B. S., & Dettmar, R.-J. 2009, *A&A*, **505**, 1
- Verheijen, M. A. W. 2001, *ApJ*, **563**, 694
- Verheijen, M. A. W., & Sancisi, R. 2001, *A&A*, **370**, 765
- Visser, H. C. D. 1980, *A&A*, **88**, 149
- Westfall, K. B., Bershady, M. A., Verheijen, M. A. W., et al. 2011, *ApJ*, **742**, 18
- Wright, S. A., Larkin, J. A., Law, D. R., et al. 2009, *ApJ*, **699**, 421
- Zaritsky, D., & Rix, H.-W. 1997, *ApJ*, **477**, 118